NTNU – Trondheim
Norwegian University of
Science and Technology

The Effect of Alloying Elements on the Ductility of Al-Mg-Si Alloys

Magnus Sætersdal Remøe

Materials Science and Engineering
Submission date: June 2014
Supervisor: Knut Marthinsen, IMTE
Co-supervisor: Ketill Pedersen, SINTEF
Ida Westermann, SINTEF

Norwegian University of Science and Technology
Department of Materials Science and Engineering

Abstract

Experiments were conducted to attempt to understand the effect of different alloying elements on the ductility of Al-Mg-Si alloys. Four alloys with different concentrations of Si, Mg, Fe, Mn and Cu were selected for examination. The strength-ductility relationship was evaluated by tensile tests, and microscopic analysis in light optical microscope, SEM and TEM was conducted to investigate grain-, constituent-, precipitatation- and fracture characteristics.

Excess-Si (Mg/Si>1.73) was found to have a detrimental effect on the ductility of Al-Mg-Si alloys, without the presence of additional alloying elements. This alloy had an elongation to fracture of 23.1%, where failure occurred partly intergranularly, and was seemingly due to poor grain boundary characteristics. Adding Fe and Cu improved the ductility (and strength) to 42.9% elongation, and the change was related to the formation of secondary-phase particles, resulting in less free Si for embrittlement of grain boundaries. The best ductility, 79.2% elongation, was found by introducing Mn, which in addition to the above-mentioned changed the recrystallization behavior.

The most desirable combination of tensile strength (456 MPa) and ductility (64.6%) was found in a balanced alloy (Mg/Si~1.73) with an addition of both Mn and Cu. Primarily, Cu was associated with an increase in strength, by changing the precipitation behavior and precipitate characteristics. Mn contributed to both an increase in strength and ductility, by forming dispersoids which influenced the recrystallization behavior, resulting in a fine subgrain structure.

Sammendrag

Eksperimenter ble utført for å forsøke å forstå effekten av forskjellige legeringselementer på duktiliteten til Al-Mg-Si legeringer. Fire legeringer med forskjellig innhold av Mg, Si, Fe, Mn og Cu ble valgt for undersøkelse. Styrke-duktilitet forholdet ble evaluert med strekktester, og mikroskopiske analyser i lysmikroskop, SEM og TEM ble utført for å undersøke korn-, partikkel-, presipiterings- og bruddkarakteristikker.

Overskudd av Si (Mg/Si=1.73) viste seg å ha en skadelig effekt på duktiliteten til Al-Mg-Si legeringer, ved mangel av andre legeringselementer. Denne legeringen hadde en forlengelse til brudd på 23.1%, og feilet delvis interkrystallinsk, noe som tilsynelatende skyltes ufordelaktige korngrensekarakteristikker. Et tillegg av Fe og Cu, førte til en betydelig forbedring av duktiliteten (og styrken) med 42.9% forlengelse, og dette ble relatert til dannelsen av sekundære partikler som resulterte i mindre fri Si til forsprøing av korngrenser. Den beste duktiliteten, 79.2% forlengelse, ble funnet ved å introdusere Mn, som i tillegg til det ovennevnte endret rekrystalliseringsatferden.

Den mest fordelaktige kombinasjonen av bruddseihet (456 MPa) og duktilitet (64.6%) ble observert i en balansert legering (Mg/Si=1.73) med et tillegg av Mn og Cu. Cu ble først og fremst forbundet med økning i styrke ved å endre presipiteringsatferd og presipitatskarakteristikker. Mn bidro til både en økning i styrke og duktilitet, ved å danne dispersoider som påvirket rekrystalliseringsatferden og førte til en finkornet mikrostruktur.

Preface

This thesis comprises studies conducted during the final semester of the 5 year Master's Degree Programme in Materials Science and Engineering at the Norwegian University of Science and Technology (NTNU). It was carried out at the Department of Materials Science and Technology, NTNU, in collaboration with SINTEF and Hydro.

It is related to a larger Hydro-project called "Smart 6xxx Alloy Development for Rolling and Extrusion" (RolEx), in which they have an R&D-collaboration with NTNU and SINTEF. RolEx is a four year project with the aim to develop new alloys and thermo-mechanical processes for extruded products and rolled plates in the 6xxx-series. These alloys are to be designed to exhibit a formability and final property balance currently not available on today's market.

The main aim of this study has been to contribute to a better understanding of the effect alloying elements have on the mechanisms controlling ductility, and in this way provide supplementary results for the RolEx project.

Acknowledgment

The accomplishment of this thesis would never have been possible without the support of several individuals, which will be presented in the following.

A special gratitude is directed at my supervisor, Professor Knut Marthinsen, for always doing his utmost with respects to the various challenges encountered during the execution of this thesis. His commitment and knowledge, along with the essential insights from my co-supervisors Ketill Pedersen and Ida Westermann, provided me with the necessary tools to carry out a study with satisfactory quality.

My appreciation goes to Morten Myren (Finmekanisk Verksted, NTNU) for his help in machining tensile specimens, and Vidar Hjelmen (SINTEF) for executing the tensile tests. I would like to thank Birgitte Karlsen (SINTEF) for her help in preparing specimens for use in TEM, and Trygve Schanche (NTNU) for his help with various needs and difficulties encountered in the metallurgical laboratory.

I am particularly grateful for the vast support I received from Yingda Yu (NTNU) in the art of operating a TEM. His dedication to educate and guide students to higher levels of understanding in the use of equipment at the SEM laboratory (NTNU) is greatly appreciated.

Finally, my gratitude goes to my fellow students for their contribution to the excellent academic and pleasant environment that has been vital for my enjoyment and development throughout these five interesting years. It is often stated that the best time of your life is experienced while you are a student, and this period of my life will certainly not be forgotten.

Table of Contents

List of figures

List of Tables

1 Introduction

Aluminum and its alloys have been known and utilized for over a century, but is still regarded as a material for the future. Its attractive properties in terms of e.g. specific strength and corrosion resistance, combined with an excellent potential for recycling, makes it appealing for numerous applications. A constant stream of innovations within the industry predicts a bright future for the light metal, and it is expected that as the alloys grow more advanced, it will increasingly take over for steel in applications formerly regarded to be out of bounds for aluminum alloys. An example is the offshore industry, which is expected to increase the use of aluminum alloys in construction applications [1].

The Al-Mg-Si series is already widely used in the automotive industry, but there is still room to improve in terms of the strength and ductility of the alloys, e.g. to ensure that they absorb a sufficient amount of the energy related to a collision. Investigations into the effect of different alloying content and thermo-mechanical processes may provide information to improve these properties.

The ductility of a material is dependent on a number of factors, which are mainly associated with microscopic characteristics. As a consequence of this, advanced instruments must be employed to examine the small-scale variations leading to different behavior. By understanding the effect alloying elements have on these characteristics it may be possible to adjust the composition and processing to obtain optimal properties.

Four alloys with different concentrations of Mg, Si, Fe, Mn and Cu were selected for experiments in this study. Tensile tests were executed to obtain the strength-ductility relationship of every alloy, and the fracture surfaces of the specimens were examined in SEM to determine the fracture mechanisms involved. In addition, it was attempted to reveal grain, constituent, and precipitatation characteristics in light optical microscope, SEM and TEM.

2 Theoretical Background

2.1 The Al-Mg-Si alloys

Aluminum alloys are separated into two main classes, cast aluminum and wrought aluminum alloys, where the latter are the most used with around 75-80% of the production quantity [2]. While cast aluminum alloys get all their strengthening through alloying elements, by solid solution and/or age hardening, wrought aluminum alloys can, in addition to this, obtain a strengthening effect through deformation hardening. The Al-Mg-Si alloys are wrought aluminum alloys with the main alloying elements being magnesium and silicon, usually with a content in the region of 0.5-1.3 wt% Mg and 0.4-1.4 wt% Si.[3]

Additional alloying elements may be added to further enhance the properties, the most commonly used being Mn (0.5-0.7 wt%), Cr (0.1-0.3 wt%) and Cu (0.3-0.9 wt%). Mn and Cr are normally introduced to prevent recrystallization and/or control grain growth during processing while the introduction of Cu increases the strength. However, using concentrations of Cu above 0.5 wt% reduces the corrosion resistance of this otherwise corrosion-resistant alloy system.[4]

The Al-Mg-Si alloys have a relatively high strength compared to the other aluminum alloy series, with a tensile strength lying in the region of 220-390 MPa. As is usual with other materials the elongation decreases with increasing strength and the tensile strain is normally in the region of 17-12% related to the above mentioned tensile strength.[3]

2.2 Processing route

Alloys from the 6xxx-series receive heat treatment after casting, and are therefore designated to temper state TX, where T indicates "thermally treated", and X is a number from 1-10 describing any possible additional treatments. The Al-Mg-Si alloys are commonly applied in temper state T6, which indicates that mechanical processing, solution heat treatment and artificial ageing to peak temper has been performed. Various events occur during these steps, and they will be properly introduced in the following subchapters.

2.2.1 Thermo-mechanical processing (TMP)

2.2.1.1 General

Thermo-mechanical processing is a collective term for processes in which the material goes through mechanical deformation at elevated temperatures; this being extrusion, rolling, forging

etc. Its origin dates all the way back to approximately 3000 B.C., when forging of bronze was used to create tools and decorative applications.[5]

The excellent mechanical properties that can be obtained in wrought aluminum alloys are highly dependent on thermo-mechanical processing to convert the material from a basic alloy with mediocre properties to one with vastly improved qualities [5]. Over 75% of all industrial aluminum alloys have in some way been through this type of processing after casting and homogenization to produce a finished or semi-finished product.[6]

Common to these processes is the creation of a complex sequence of deformation in the material, which along with prior and subsequent heat treatment steps, changes both the microstructure and texture of the material. As these characteristics have a great effect on the material properties, it is of vital importance to understand their mechanisms to be able to predict the final properties of the alloy.[7]

2.2.1.2 Extrusion

All the alloys involved in this thesis have been extruded from a billet after casting and homogenization. Extrusion is generally a cheap process which has relatively short operating times and a variety of alloys may be formed into complex shapes. As an effect of this, around 30% of aluminum alloys consumed world-wide are extruded products, and over 90% of these are estimated to come from the 6xxx-system.[6]

As depicted in Figure 2.1, the course of a typical Al-Mg-Si alloy from molten aluminum to finished product goes through many steps. After casting, the material is heated and kept at an elevated temperature to level out local differences in e.g. concentration and particle distribution caused by solidification, and is therefore referred to as homogenization. Thereafter, the billet is preheated to the desired extrusion temperature, extruded, and consequently cooled. Finally the product is heat-treated to increase the hardness of the product by age hardening.

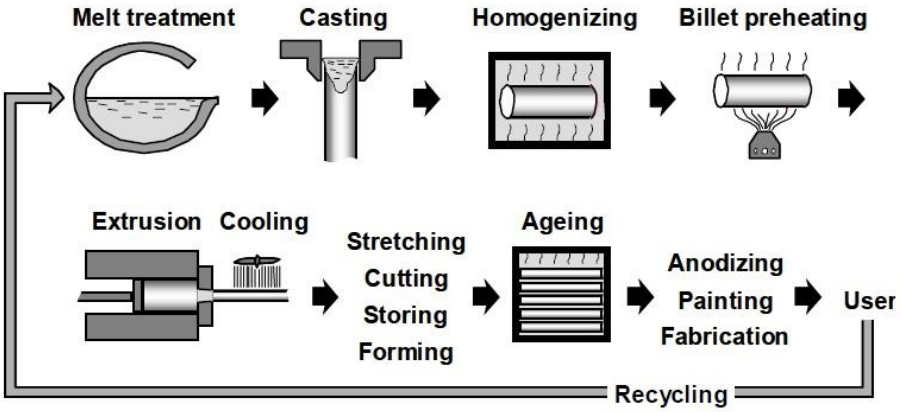

Figure 2.1: Production process. A schematic description of the production process of a 6xxx-alloy from casting to finished product [6].

The extrusion process itself is illustrated in Figure 2.2, where a billet is placed in a chamber with a die in one end and a ram in the other. The billet is forced through the relatively narrow die and is converted into extended profiles with dimensions defined by the geometry of the die. To reduce the load and wear of the dies, extrusion is normally performed at elevated temperatures where the materials usually exhibit better formability [5]. The extrusion temperature typically ranges between 500-550°C for aluminum alloys.[8]

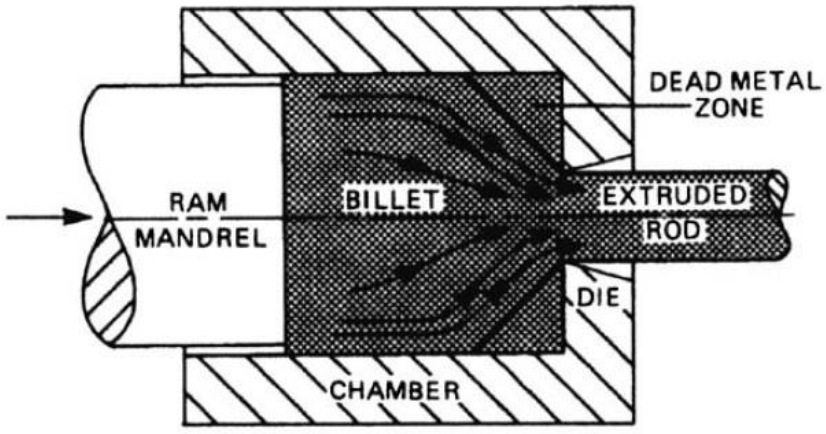

Figure 2.2: Extrusion process. An illustration of how an extrusion process is executed [5].

The heat-treatment process varies from alloy to alloy, as the temperatures and holding times chosen are dependent on the characteristics of the material. Wrought aluminum alloys are typically solution heat treated after TMP and thereafter age-hardened at a lower temperature [6]. A qualitative description of the different heating stages an alloy as the ones involved in this

project follows is given in Figure 2.3. An alloy following this type of processing is said to be in the temper state T6 after ageing.[9]

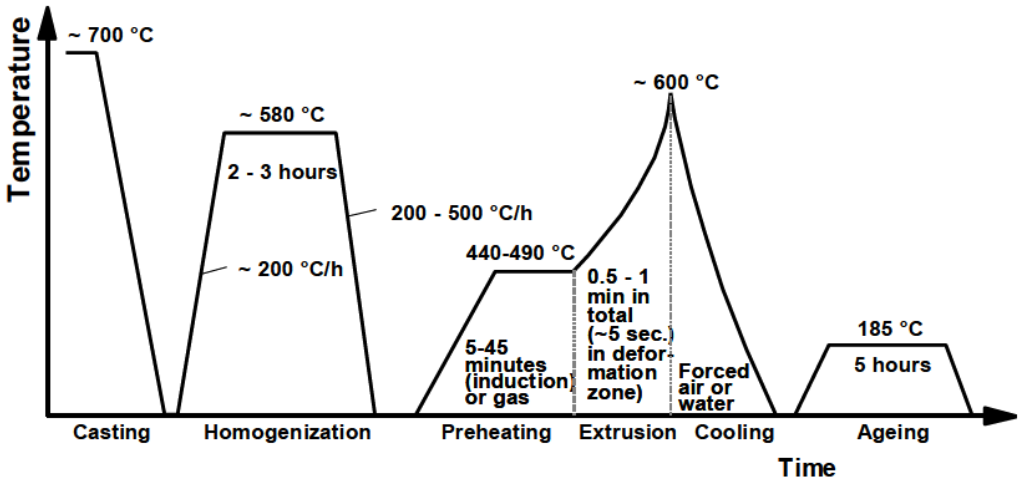

Figure 2.3: Temperature/time profile. A qualitative description of the different temperature and time intervals a given 6xxx alloys follows [6].

2.2.2 Microstructure development

2.2.2.1 Formation of second phase constituents during casting

As a result of the solidification process, second-phase constituents, in the form of intermetallics, may be found in the material after casting. The constituents may be divided further into two categories, depending on their ability to dissolve during homogenization.

Non-soluble constituents are mainly Fe-containing, as Fe has an almost negligible solubility in the aluminum matrix (~0.04 wt% at 655°C [10]). They may therefore not dissolve, but during homogenization they may transform into different phases. Fe is usually an unwanted element in aluminum, but is almost always present as an impurity in Al-Mg-Si alloys, due to the difficulty associated with removing it completely from the molten metal.[11]

Compounds without Fe may be highly soluble, depending on the alloying content. One of the purposes of homogenization prior to thermo-mechanical processing is to dissolve these constituents. During homogenization, equilibrium phases grow by diffusion from a super-saturated matrix, and due to the liberation of alloying elements from the soluble constituents, while metastable particles are transformed to equilibrium particles.[11]

Typically, these particles are broken and divided into smaller pieces during mechanical processing, and aligned with the working direction. In tension, they are known to be damaging

to the fracture toughness of the materials, due to their cracking at low strains. Commonly 25-50% of these particles crack after 7% plastic strain in tension for high-strength alloys.[11]

Depending on the solidification rate and alloying content, different types of constituents may form during the casting of 6xxx alloys. G. Sha et.al. discovered both cubic α-AlFeSi and β-AlFeSi after solidification of a 6082 alloy, where the former seemed to be observed at a higher frequency at higher growth rates, and the latter at lower growth rates [10]. The α-AlFeSi was found to have a composition close to $Al_{12}Fe_3Si$, while the β-particle is assumed to be Al_5FeSi. The latter is known to result in poor ductility and formability.[10, 12]

The introduction of Mn has been shown to change the conditions for constituent formation in 6xxx alloys, leading to the formation of α-$Al_{15}(FeMn)_3Si$ and Al_9Mn_3Si, in addition to the above mentioned. In the Al-Mg-Si-Cu alloy system, other constituents have been observed after casting, these mainly being $Al_{1.9}CuMg_{4.1}Si_{3.3}$, $Al_5FeMnSi$ and $Al_8(FeMn)_2Si$ for an alloy containing 0.3 wt% Fe. The $Al_{1.9}CuMg_{4.1}Si_{3.3}$ was found to completely dissolve during homogenization, while it was also found that increasing the Mn content leads to an increasing amount of AlFeMnSi particles on the expense of $Al_{1.9}CuMg_{4.1}Si_{3.3}$.[13, 14]

2.2.2.2 Deformation structure

The microstructure of the material will be subject to drastic changes during mechanical processing, due to the substantial forces involved. The microstructure of a material may be generalized into two categories, one being the phase and grain structure, and the other the defect structure.

The defect structure may be broken down into different types of defects, with some of them summarized below.[5]

- Composition defects: Segregation of alloy elements and local differences in composition.
- Point defects: Vacancies and interstitial/substitutional atoms.
- Line defects: Dislocations.
- Planar defects: Grain and phase boundaries and stacking faults.
- Volume defects: Pores and inclusions.

Most of the energy that is generated during the deformation process is released as heat, but anything from 1-10% of the energy may be stored in the structure of the material, as point defects or dislocations [5]. Point defects are of less importance here as the mobility of vacancies is high at higher temperatures, which allows them to continuously annihilate point defects like

interstitials through diffusion. As a consequence, almost all the energy stored is related to the accumulation of dislocations, and their orientation and distribution is the most vital difference between the material prior to, and after annealing.[15]

The amount of dislocations increase if the dislocation generation and multiplication occurs faster than dynamic recovery is able to annihilate them. The increase in dislocation density is due to a continuous obstruction of newly formed mobile dislocations, and the way these dislocations interact with the deformation structure. The grains change shape according to the macroscopic change in the subject's dimensions during extrusion, causing the grains to become elongated and the grain boundary area to increase. This area needs to be created during the extrusion process, which is done by the inclusion of some of the dislocations generated during deformation. The increased energy stored may therefore be associated with the increase in grain boundary area.[15]

During deformation the dislocations may move an average distance L, and the dislocation density is related to the true strain by the following expression:

$$\varepsilon = \rho b L \qquad 1$$

Where ε represents strain, b the burgers vector, and ρ the dislocation density. There is no unambiguous determination of what to use as a value of L, but it may be justified in some cases to relate it to e.g. the grain size or the average particle distance.[15]

The microstructure that develops during extrusion normally consists of elongated grains with a high defect density, which are generally more deformed near the surface than in the middle. The grains contain an internal substructure, which again are finer in regions subjected to larger strains. An illustration of how and why the deformation varies across the cross-section may be seen in Figure 2.4, where the deformation structure is captured at some stage during the extrusion process.[16]

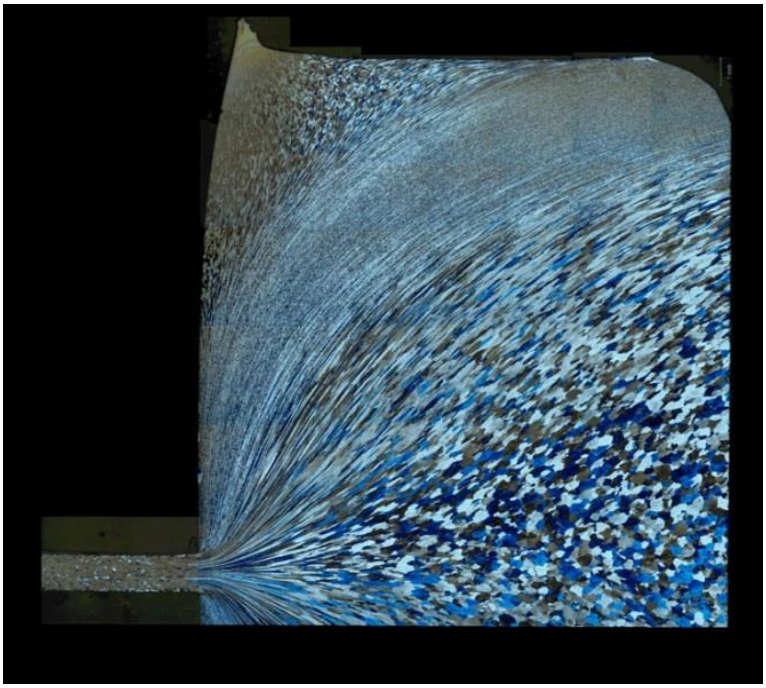

Figure 2.4: An image of the deformed microstructure during extrusion (Printed with the permission of Trond Furu, Hydro Aluminum)

Different substructures may arise during deformation, depending on the material and the parameters of the process. Aluminum has a high stacking fault energy (170 mJ/m^2), leading to the creation of cellular substructures rather than twins and stacking faults. The substructures that develop are temperature dependent. At low temperatures cellular structures are likely to form, while at higher temperatures sub-grains with narrow well-defined walls are the most likely.[2]

2.2.2.3 Recovery and recrystallization

The deformation structures during or after thermo-mechanical processing are thermodynamically unstable, such that subsequent annealing of the subject leads to an evolution in the sub-structure. This is controlled by thermally activated processes, which decrease the stored energy of the structure and thereby also decrease the hardness. This evolution of the sub-structure may also take place during deformation, and is typical for aluminum. It is then called dynamic recovery and dynamic recrystallization.

The processes leading to the changes during heat-treatment (or extrusion) may be separated into three categories.[5]

- *Recovery* is driven by the stored energy in the structure and is related to micro-mechanisms which move and annihilate point defects and dislocations, e.g. arranging them in sub-grains.
- *Recrystallization* is also a process driven by the stored energy in the structure, but is related to the movement of high-angle boundaries.
- *Grain growth* is driven by the surface energy of the grain boundaries and is, as for recrystallization, related to the movement of high-angle boundaries to reduce the total stored energy.

The relationship between the relative amount of recovery and recrystallization occurring is dependent on several factors, e.g. strain, annealing temperature and material. In general, recovery is the dominant mechanism at lower temperatures and as the temperature increases recrystallization becomes more dominant. However, even at high temperatures some recovery will occur prior to recrystallization.[5]

Recovery in aluminum proceeds with most of the dislocations being annihilated or rearranged into walls which lead to the creation of well-defined sub-grain boundaries within each grain. The amount of recovery is highly dependent on the stacking-fault energy of the material, where a higher stacking fault energy, as is the case for aluminum, increases the likelihood of recovery. This is an effect of the ease by which cross-slip and local annihilations in the material may occur.[2]

At higher temperatures recrystallization is more dominant and involves the nucleation and growth of new grains within one and the same phase. The most common sites for nucleation in aluminum are particles and transition bands.[5]

Transition bands are created when two neighboring volumes within a grain deform on different slip systems and rotate to give different orientations. Particles, preferably with sizes above 1 μm, create a deformation zone that surrounds it, and which may trap mobile dislocations. The dislocation density (ρ) associated with such deformation zones is given by,

$$\rho = \frac{3F_v s}{rb} \qquad 2$$

where F_v is the volume fraction of particles, r the size of the particles, and s and b the shear strain and burgers vector respectively. The phenomenon is called particle-stimulated nucleation (PSN), and it's the large differences of stored energy in these zones that stimulate recrystallization.[5]

2.2.2.4 Dispersoids

When transition metals, such as manganese, are present in 6xxx-alloys, they tend to form small particles or precipitates during casting or homogenization. Due to their slow diffusivity in the aluminum matrix, these particles, or dispersoids, are usually smaller than 1 μm and widely dispersed. Depending on factors such as size and distribution, which are mainly effects of alloying content and homogenization treatment, they may have beneficial effects on the recrystallization and deformation behavior [11]. At lower temperatures, for shorter times, the dispersoids tend to be small and widely dispersed, while at higher temperatures, for longer times the relation is reversed.[17]

Dispersoids are known to delay or hinder recrystallization during processing and as they are often oriented in the direction of working, they tend to pin grain boundaries, aiding to retain the fibrous grain morphology. Their ability to control the grain structure is highly dependent on size, spacing and coherency, e.g. small dispersoids of less than 0.4 μm may hamper discontinuous recrystallization by pinning of subgrains, and thus preventing recovery. Coherent dispersoids are more effective in this regard, as they force the necessity to change the dispersoid-matrix interface from coherent to semi-coherent or incoherent, a process requiring high energies.[11]

In high-purity Al-Mg-Si-Mn alloys, the formation of AlMnSi dispersoids is known to occur, while the presence of iron leads to the formation of a quaternary Al(Mn, Fe)Si phase. It has been suggested that they tend to nucleate on β'-Mg_2Si particles via an intermediate secondary phase, and precipitate from around 400°C. Strobel et.al found that the dispersoid phases seem to be α-$Al_{12}(MnFe)_3Si$ when the Mn/Fe ratio is less than 1.6, and if larger, α-$Al_{15}(MnFe)_3Si_2$ [17]. In another research Matsuda et.al identified the presence of coarse AlFeSi dispersoids in transition metal bearing alloys with and without Cu [18].

2.2.3 Age hardening

2.2.3.1 Hardening by precipitation

In addition to strengthening effects caused by grain size, dislocation density, texture etc., the alloy may be further strengthened by age hardening. This involves the precipitation of finely distributed particles into the matrix from a super-saturated state. For this to occur the material must have a decreasing solubility of alloy elements with decreasing temperatures. A phase diagram showing the decreasing solubility of Mg and Si with temperature, represented by the phase Mg_2Si, is given in Figure 2.5 below. [2]

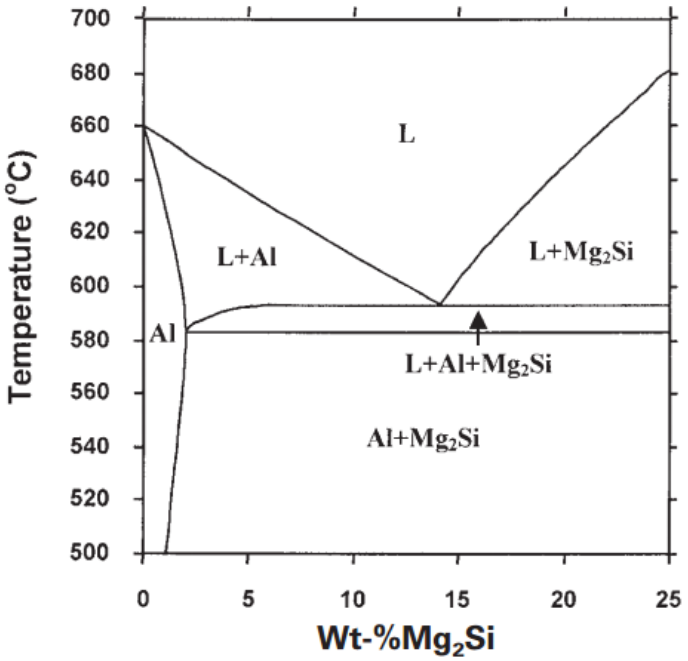

Figure 2.5: A phase diagram showing the solubility of Mg and Si in the Al-matrix at different temperatures [19].

Age hardening is a three step process where the alloy first must be annealed at a temperature above the solvus line to dissolve alloy elements from particles, and consequently quenched to keep the alloy elements in a super-saturated aluminum matrix. By controlling the time and the temperature of the next heat treatment stage, the decomposition of the super-saturated solution will result in finely dispersed precipitates which inhibit dislocation movement. The level of strengthening is dependent on the distribution of precipitates in the matrix, and its coherency. While incoherent precipitates may be passed, coherent precipitates may both be cut and passed. The superior ability of a coherent precipitate to inhibit dislocation movement is down to several factors, among which are; the introduction of a strain field in the matrix due to coherency and the increased surface area resulting from cutting.[3]

In the Al-Mg-Si alloys the precipitation sequence follows the development described below, and illustrated in Figure 2.6, with the precipitated particles following different compositions of the formula Mg_xSi_y:

$$SSSS \rightarrow atomic\ clusters \rightarrow GP\ zones \rightarrow \beta'' \rightarrow \beta', \mathrm{U1}, \mathrm{U2}, \mathrm{B}' \rightarrow \beta\ [20] \qquad 3$$

Each stage shown above represents intermediate steps during the precipitation process where the particles are precipitated in different sizes, compositions and structures. The strengthening effect of the precipitates is dependent on their ability to resist the dislocations from cutting

through their structure. The GP-zones and β'' phases are partially coherent, meaning they are shearable, with a needle shape. β' has also been found to be partially coherent, but precipitates in the shape of a rod. The equilibrium phase β precipitates as incoherent plates, and is thus non-shearable and dislocations are forced to loop around the precipitates.[3]

The strengthening effect is thought to be strongest for the β'', and has been proposed to be caused by the high energy of which is needed to break the Mg-Si bands, along with the shape and size effects [3]. There may be various other intermediate phases present at different ageing times, but these are the most common.

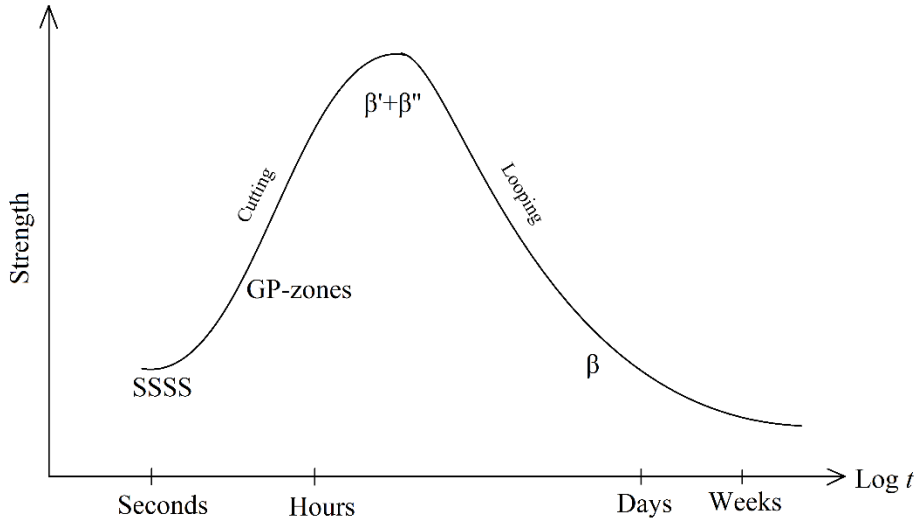

Figure 2.6: The precipitation sequence of an Al-Mg-Si alloy related to strength and time [21].

2.2.3.2 The influence of the Mg:Si ratio

The ratio of the Mg- and Si-content is of importance in the 6xxx-series. The properties may be optimized by adjusting the content ratio of Mg and Si. A balanced 6xxx alloy usually exhibits the best balance of properties given the alloy mainly consist of only these two elements. These balanced alloys have a ratio of Mg on Si approximately equal to 1.73, and if the concentration of Si increases in relation to this it is called an excess Si alloy.[22]

In alloys for automotive applications, excess Si alloys have been widely used to improve the age hardening response [23, 24]. The presence of excess Si has not been found to change the precipitation sequence, structure and lattice parameters of the metastable precursor phases in Al-Mg-Si alloys. However, studies have shown that it may result in a modification of the composition, especially in the early stages of precipitation, and change the density of

precipitated particles. Gupta et.al found that excess Si alloys had reduced times to initiate a strengthening response during ageing as compared to that of the balanced alloys [23]. This was concluded to be due to the amplified precipitation of fine, widely dispersed β''. The reduction in Mg/Si ratio in zones and clusters was found to lead to increased precipitation and strengthening [23, 25]. The presence of excess Si has, however, been found to reduce the ductility of Al-Mg-Si alloys. Aucote and Evans found that a significant amount of the excess Si participated in the formation of pure Si particles on the grain boundaries, leading to intergranular fracture [25].

2.2.3.3 The effect of Cu on precipitation

Due to the increased importance of 6xxx alloys in the automotive industry, various studies have been conducted on the precipitation behavior of Al-Mg-Si alloys in the presence of Cu. Although many of the mechanisms and intermediate phases involved are still unclear, there is evidence that the presence of Cu changes the precipitation behavior significantly.[26]

As mentioned above, an increase in the strength of Cu-free excess-Si alloys has often been observed for increasing Si-content, and the strengthening effect has been ascribed to an increase in the volume fraction of β''-particles. In excess-Si alloys containing Cu however, TEM imaging has shown that with an addition of 0.3 wt% Cu the β''-precipitates observed at peak strength only amounted to 20-30% of the total amount of particles. The remaining particles had needle or plate morphologies and consisted of Cu-containing GP zones and precursory phases for Q', a phase observed at later stages in ageing with the presence of Cu. These precursory phases were present in the shape of needles and plates, and are assumed to give a significant strengthening effect to Cu-containing Al-Mg-Si alloys at peak strength, especially the lath or needle shaped L phase [26, 27]. At early stages in the ageing process, needle-shaped and fully coherent GP zones have been observed, and that did not have the pre-β'' monoclinic structure typical for GP zones in excess-Si alloys without Cu.[27]

The presipitation sequence with an addition of Cu is currently assumed to be

$$SSSS \rightarrow atomic\ clusters \rightarrow GP\ zones \rightarrow \beta'', Q', L, S, C, QC \rightarrow Q' \rightarrow Q \text{ [28]} \qquad 4$$

where L, S, C and QC are all precursory phases for Q'. The chemical composition of both Q' and Q is expected to be $Al_3Cu_2Mg_9Si_7$, while it is still unknown for the precursory phases.[27]

2.2.3.4 The effect of age hardening on electrical conductivity

There is a relation between the amount of solute that has been precipitated, and the electrical conductivity of a material. In general, defects and impurities in the matrix decrease the electrical conductivity of a material as the disturbances makes it more difficult for electrons to move. As particles are precipitated from the super-saturated matrix, the amount of impurities decreases, and thus the electrical conductivity generally increases. The conductivity may therefore be used as a measure of the precipitation development during ageing, and should follow a similar behavior as what would be observed when measuring the strength of the specimen as a function of ageing time.

With the presence of Mg, Si, Fe and Cu, the effect on the electrical conductivity by these foreign elements in solid solution may be given by Matthiessen' rule:

$$\frac{1}{\kappa} = 0.0267 + 0.032Fe_{ss}\% + 0.0068Si_{ss}\% + 0.0051Mg_{ss}\% + 0.0033Cu_{ss}\% \qquad 5$$

where κ is the electrical conductivity, and Fe_{ss}%, Si_{ss}%, Mg_{ss}% and Cu_{ss}%, the weight percent of the respective elements in solid solution.[29, 30]

2.2.3.5 Precipitate free zone (PFZ)

Precipitation free zones emerge in all age-hardenable alloys and appear as zones drained of precipitates, along the grain boundaries. They occur mainly due to mainly two reasons.

1. As a result of the easy diffusion of alloying elements to the grain boundaries, a narrow zone of ~50 nm is formed on either side of the boundary. The alloying elements subsequently combine to form relatively coarse particles on the grain boundaries.
2. There is a depletion of vacancies near a grain boundary, which retards the nucleation of precipitates at a given ageing temperature, due to the difficulty for alloying elements to diffuse. Some precipitates, such as GP-zones, may be less dependent on the vacancy concentration, and will thus not be significantly affected.

There are ways in which one may reduce the effect of the depletion of vacancies. At higher solution heat treatment temperatures and with faster quenching the excess vacancy concentration increases and leads to a reduction in the width of the PFZ. Ageing at lower temperatures may also have a positive effect, as it allows for smaller nuclei to be stable.[2]

Apart from the detrimental effect of the grain boundary particles, the presence, and the width in particular, of the PFZ is an important property in age-hardenable alloys. Plastic flow may occur with more ease along PFZ's since these areas are softer than the surrounding matrix [31,

32]. Deformation in the PFZ may lead to the pile-up of dislocations at grain boundary precipitates or grain boundaries and form microvoids leading to cracks and fracture.[33]

2.3 Tensile tests

2.3.1 Stress-strain curves

To evaluate the mechanical properties of a material, the uni-axial tensile test is commonly used. The tensile test applies a uniaxial force to the material to measure the strength and ductility in a given direction. As the work hardening of the material increases as the material is stretched, resulting in a higher resistance to tension, the tensile force is increased with a quantity related to the strain rate. The observed stress is plotted against the observed strain in the well-known stress-strain curve, illustrated in Figure 2.7 below.

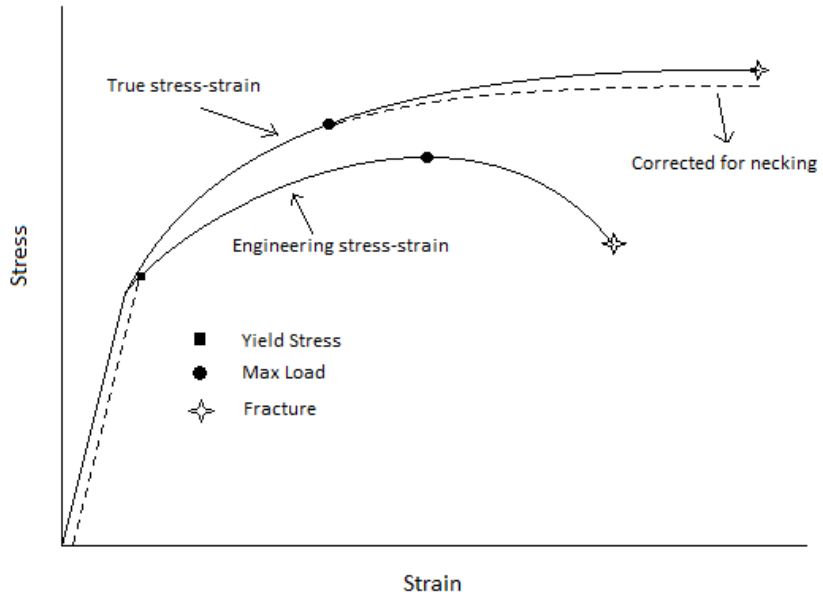

Figure 2.7: Stress-strain curves. The stress-strain relationship, illustrated both by the engineering stress-strain curve and the true stress-strain curve [21].

2.3.1.1 Engineering vs. true stress

As is shown in Figure 2.7, there are two ways to look at the stress strain relationship of a material. When calculating the engineering stress (s), the applied force (P) is related to the original cross-sectional area (A_0) of the specimen.[21]

$$s = \frac{P}{A_0} \tag{6}$$

As the cross-sectional area in fact decreases as the material is strained, a more precise relationship is given by the true stress-strain curve (σ-ε), where the cross-sectional area (A) is updated continuously during the tension test. The true stress may be calculated and related to the engineering stress and strain by the following expression

$$\sigma = \frac{P}{A} = s(1+e) \tag{7}$$

where e is the engineering strain. Similarly, the true strain is calculated and related to the engineering strain through

$$\varepsilon = \ln\left(\frac{L}{L_0}\right) = \ln(e+1) \tag{8}$$

where L is the length of the specimen at a given time, and L_0 the original length. Initially, when strains are low, there is no plastic deformation occurring in the material. This elastic region of the curve is indicated by the straight line at low strains. The transition to plastic deformation is shown by the point where the curve abruptly becomes non-linear, and work hardening is initiated. The two curves, for s and σ, deviate more and more as the cross-sectional area decreases. [21]

The maximum strength of the material is related to the point of maximum load. After this point a neck will develop in the tensile specimen, and the cross-sectional area will now start to deform non-uniformly. Neither of these graphs show the true development after this point as the stress and strain must be corrected for this deviant behavior [21].

2.3.1.2 Bridgman correction

A triaxial stress state is introduced in the necked region, resulting in a higher registered stress than what would actually be present if uniaxial stress conditions still prevailed. An expression keeping in mind this new stress state was provided through the Bridgman analysis [34]. The analysis is based on four main assumptions, being

- the arc of a circle may approximate the outline of the neck.
- the necking region's cross-section stays circular during the test.
- von Mises' stress yield criterion is applicable.
- the strains along the cross-section are constant.

which lead to the following corrected stress equation

$$\sigma = \frac{(\sigma_x)_{avg}}{(1+2R/a)[\ln(1+a/2R]} \quad 9$$

where σ is the corrected stress, $(\sigma_x)_{avg}$ is the measured stress in the axial direction, R is the curvature and 'a' is the radius of the neck [21]. These parameters are illustrated in Figure 2.8 below.

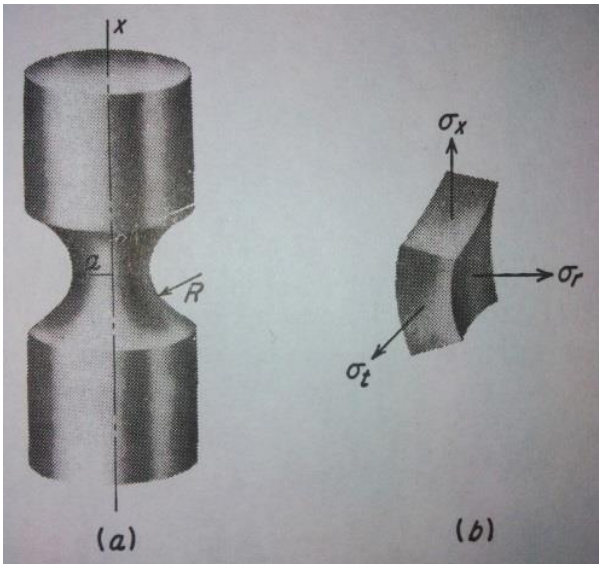

Figure 2.8: The necking region. a) An illustration of the geometry of a necking region. b) A triaxial stress distribution [21].

Due to the relative difficulty with which one is able to measure the radius and the curvature of the neck, an approximation to the ratio of a/R has been modelled [35]. Le Roy et.al proposed the following relationship

$$\frac{a}{R} = 1.1(\varepsilon_p - \varepsilon_u) \quad 10$$

where ε_p is the plastic strain at a given point after necking, and ε_u the strain at necking [36].

2.3.1.3 Laser extensometry

In the stages of a tensile test preceding necking, the strain may be measured using standard contact extensometers, e.g. clip-on extensometers. The extensometer arms are clipped on to the tensile specimen, and the distance between the arms increases as the specimen is stretched, thus measuring the strain through elongation. However, after necking occurs, the decreasing area in

the neck induces a larger stress in this region relative to the original cross-sectional area. A laser extensometer may be used to measure the increase in strain after necking as it gives a measurement of the decrease in cross-sectional area, or more precisely, its diameter [37]. The diameter at a given time or strain during the tensile test is compared to the original diameter, and the average true axial strain may be calculated through

$$\left(\varepsilon_x\right)_{avg} = \ln\left(\frac{A_0}{A}\right) \tag{11}$$

where $(\varepsilon_x)_{avg}$ is the strain, A the area at a given time, and A_0 the original area [38]. The shape of the neck is usually assumed to be elliptic [39, 40], and the area is calculated through two diameters measured perpendicular on one another, leading to

$$A = \frac{\pi}{4} D_1 D_2 \tag{12}$$

2.3.1.4 Toughness

A measure of the toughness of the material may also be extracted from the stress-strain curve. The toughness may be defined as the ability to endure occasional stresses above the yield stress without fracturing [21]. The area under the curve in the stress-strain plot gives a measure of the amount of work per unit volume that the material may be exposed to without fracturing. For a ductile material this property may be approximated by the following expression.

$$U_T = \frac{s_0 + s_u}{2} e_f \tag{13}$$

Where U_T is the toughness, s_0 the engineering yield stress, s_u the engineering tensile stress and e_f the engineering strain at fracture.[21]

2.3.2 Fractography

After performing a tensile test one is often interested in obtaining a better understanding of the mechanisms behind the fracture. Fractography is the study of the nature of a fracture from the microscopic investigation of the fracture surface. The examination is most commonly performed with the use of a scanning electron mictroscope (SEM), due to its impressive depth of field. The use of SEM for fractography will be presented in section 2.4.

Several fracture modes may be observed through the effect they have on the fracture surface characteristics. The mechanisms and resulting surface characteristics of cleavage, intergranular fracture, and dimpled rupture are summarized below.

- **Cleavage** fracture is a brittle fracture mode occurring along specific crystallographic planes. They may be observed as facets generally of the same size as the grain in which it has propagated. "River markings" are often observed in such fractures, and may be discovered as plateaus and connecting ledges caused by the crack moving along a number of parallel planes.
- **Intergranular fracture** may occur at weak grain boundaries with the presence of impurities such as second phase particles at grain boundaries, grain boundary corrosion, a wide PFZ etc. The crack moves along the grain boundaries and intergranular fracture is characterized by a "rock candy" surface appearance.
- **Ductile rupture** creates cup-like pits on the surface, due to the formation of micro-voids. Its mechanisms will be explained in the following section.[21]

2.3.2.1 Ductile fracture

Ductility may be defined as the extent to which a material may be deformed prior to fracturing [41]. This property is thus directly affected by factors that influence plastic flow, such as strain rate, temperature, particles, grain sizes etc. One usually refers to fracture types as being ductile or brittle.

Ductile fractures occur at deformations significantly higher than the tensile elongation, the beginning of neck formation. It usually starts by the nucleation of voids in the center of the neck where the stress is the largest, and as deformation continues the internal voids grow and eventually coincide by the necking and rupture of areas between them. This internal fracture grows until the outer rim fails to support the load, and the edges collapse by sudden shear, creating the "cup and cone" geometry of the specimens' fracture surfaces. The voids are usually nucleated at particles as the interfaces between particle and matrix are weak or the particle itself is weak or brittle.

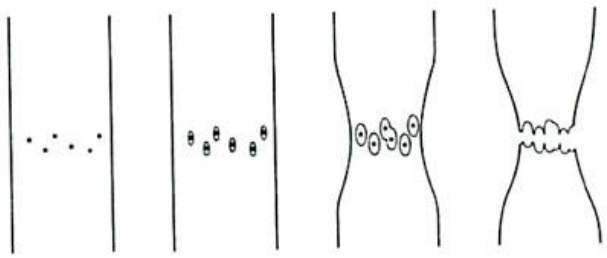

Figure 2.9: Illustration of the development of a ductile fracture [21, 42].

The more particles in the alloy, the shorter the distance between them, and thus the ease by which the voids may link up, normally causing a decrease in ductility. Another factor that may be important is the presence of an alignment of particles in forged materials which may cause failure along "flow lines", though this is not assumed to be a significant problem if the loading occurs in the extrusion or rolling direction.[43]

2.3.2.2 Brittle fracture

Brittle fractures give a different surface texture than the ductile fractures with the presence of facets as a result of e.g. cleavage or grain boundary fracture.

Cleavage occurs by slip on certain crystallographic planes unique for a given material and crystal structure. It initiates when the stress exceeds the following limit

$$\sigma_a = \sigma_c / \cos^2 \phi \qquad 14$$

where σ_a is the applied tensile stress, σ_c is the critical normal stress across the cleavage plane, and ϕ is the angle between the tensile axis and the plane normal. However, fracture in polycrystals may not happen exclusively by cleavage, as the cleavage planes in one grain does not necessarily link up with one in a neighboring grain. This contributes to explaining the preference of small grains in the material.

Brittle grain boundaries may be susceptible to fracture as they form easy fracture paths. This brittleness may be inherent in the material or caused by other factors such as the segregation of impurities to the grain boundaries or the presence of a thin film of a brittle second phase.[43]

2.4 Scanning electron microscope (SEM)

2.4.1 Backscatter electron imaging (Z-contrast)

When the electron beam hits the sample surface, a number of signals may be detected, such as secondary electrons, backscattered electrons, x-ray radiation, auger electrons etc. The electron scattering may be separated into two groups, namely elastic and inelastic scattering. Backscatter electrons belong to the former, and results from the interaction of incident electrons with atom cores. The energy loss related to this scattering mode is found to be negligible, thus the name elastic.

The probability of elastic scattering is proportional to $(Z/E)^2$, where Z is the atomic number of the scattering atom, and E the energy of the incident atom. The so-called Z-contrast is a consequence of this relationship, as atoms with a higher atomic number is more likely to scatter,

giving a stronger signal in the detector. Due to the higher number of electrons hitting the detector from an area with a higher atomic number, this area will appear brighter than its surroundings.[44]

2.4.2 Fractography

The depth of field of the microscope is vital when studying fracture surfaces, and this is the reason why SEM is the preferred choice. It has a far superior depth of field than e.g. a light microscope due to a smaller beam divergence, among other important variables. The depth of field may be defined as the maximum height difference in the sample where the image may be in focus. The depth of field in SEM is often denoted as D, and as long as the height difference in the sample is smaller than D the different areas of the sample may be in focus. This height difference may be calculated through

$$D = \left[\frac{\delta}{M} - d_p \right] \cdot \frac{1}{\alpha} \qquad 15$$

Where δ is the resolution of the eye, M the magnification, d_p the electron optical resolution, and α the beam divergence.

The depth of field and resolution of the SEM improves on the expense of one another, and one is forced to compromise. An increase in the working distance improves D as it causes a decrease in α, but this will in turn worsen the resolution. Another way to increase D is to choose a smaller aperture, although this may require the use of a higher current. As the resolution (Eq. 16) is proportional to the square root of the beam current, it will increase, leading to poorer resolution.[44]

2.4.3 Energy dispersive spectrum (EDS)

EDS makes use of the X-ray radiation emitted when the electron beam penetrates the sample surface, to quantify the chemical composition of the sample area. X-ray radiation is emitted in two ways; the retardation of electrons in the electro-static field around the atoms, or from the ionization of the atoms. The former results in a continuous spectrum regarded as noise, while the latter yields a characteristic spectrum which provides information about the specific atoms present.

The energy associated with the emitted x-ray is dependent on both the atomic number and the electron shell it originates from. As the energy of a photon is inversely proportional to its wavelength, the relation may be written as

$$\lambda = K / (Z - \sigma) \quad 16$$

where λ is the wavelength, and K and σ constants related to the shell the radiation originates from.

To achieve precise results, one must be aware of the actual volume analyzed. The area of the surface interacting with the electron beam is given by the resolution

$$d = k\sqrt{\frac{i}{E_0}} \cdot \frac{1}{\alpha} \quad 17$$

where k is a constant related to the cathode material, i is the beam current, and E_0 the energy of the incident electrons. As a lower atomic number results in a deeper penetration depth of the incident electrons, Z is part of the expression for the depth from which x-rays may be emitted from. The penetration depth may be approximated through

$$R_{BS} = 8.3 \cdot 10^{-3} \cdot A \cdot E_0^{1.67} / (Z^{0.889} \rho) \text{ [44]} \quad 18$$

where Z is the mean atomic number, A the atomic weight, and ρ the density of the material. [44]

2.5 Transmission electron microscope (TEM)

Equal to the SEM, TEM uses electrons instead of light to form an image. As is indicated in the name, the electrons are required to pass through the sample, to enable the microscope to yield results. The ability of an electron to pass through the sample is dependent on its energy, and thus the acceleration voltage of the microscope (Eq. 18). The resolution is also dependent on the acceleration voltage, as an increase in its value results in a smaller wavelength of the electron. In general, the TEM is usually applied in diffraction mode or microscope mode, although it has other possible functions.

As the electrons pass through the sample, they get scattered by elastic or inelastic processes, similar to what happens with backscattered electrons and secondary electrons in SEM, respectively. While using diffraction and microscope mode, the inelastic electrons only contribute to create background noise in the image, and are therefore not of particular interest [45]. The TEM is built up of several levels of focusing lenses, and a schematic illustration of the electron pathway from filament to screen in a conventional TEM is shown in Figure 2.10.

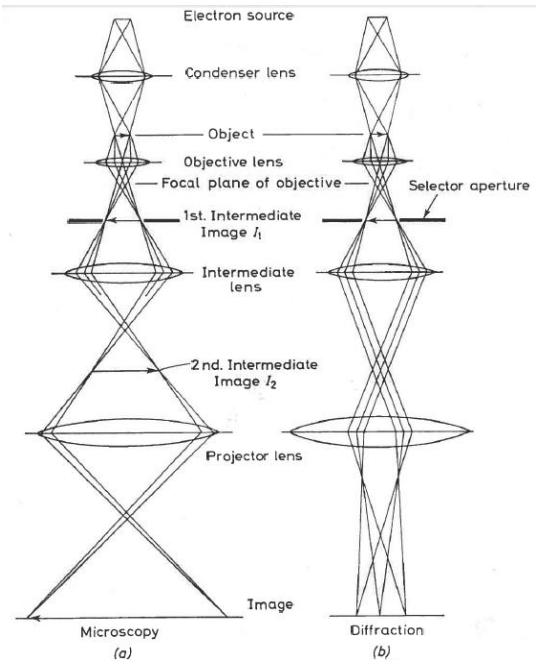

Figure 2.10: The pathway of the electron beam through the TEM in a) microscopy mode, and b) diffraction mode [45].

2.5.1 Diffraction and imaging

Due to the systematic way in which the atoms are oriented in the crystal, the scattered electrons will interfere constructively and destructively in certain directions. In analogy with what happens to a laser beam scattered by an optical grid, the atomic planes in the crystal lattice induce constructive and destructive interference on the electron beam in directions where the path difference is equal to an integer multiplication of the electron's wavelength. This path difference amounts to the interplanar distance in the lattice, and the relation may be expressed mathematically through Bragg's law:

$$2d \sin\theta = n\lambda \qquad 19$$

where d is the interplanar distance, θ the incident angle, λ the wavelength and n the order of diffraction.[45]

In diffraction mode the diffraction pattern is magnified on to a fluorescent screen, and may reveal important information about e.g. the nature of the material or the orientation of the grain relative to the incident beam. As illustrated in Figure 2.11, the parallel beams resulting from diffraction conditions satisfying Braggs' law, are focused in the focal plane by the objective lens, thus creating a diffraction pattern.[45]

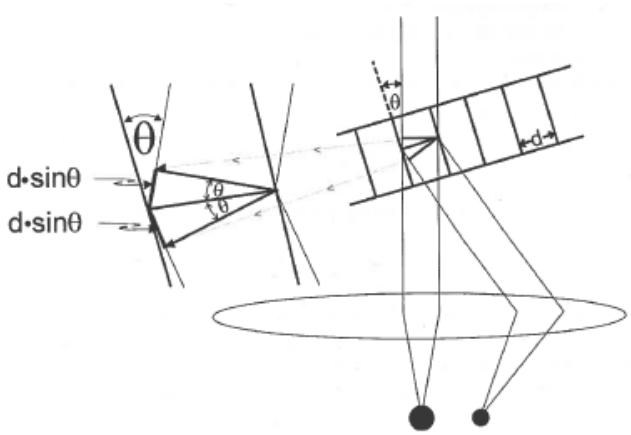

Figure 2.11: An illustration of Braggs' law [45].

When using microscope mode, all the radiation leaving the same point in the sample is focused in the image plane of the objective lens, and magnified on to the fluorescent screen creating an image. To change between the two modes, one must change the strength of the intermediate lens. As may be seen from Figure 2.12, the intermediate lens in microscope mode gives a more abrupt reflection of the beam, and is thus stronger.[45]

Figure 2.12: The pathway of the electron beam through the intermediate lens to the image plane. The beam is deflected stronger by the intermediate lens [45].

Although Braggs law implies that only one reflection may be obtained from a certain set of planes at the same time, one may usually observe a pattern with reflections from several orders "n", from the same lattice. This is why one is able to observe the familiar diffraction patterns as shown by the example in Figure 2.13b, and comes as a result of mainly three causes [45]:

1. The incoming beams are not completely parallel.
2. The sample is always somewhat bent (Figure 2.13a).
3. In such a thin sample, deviations from Braggs law may occur.

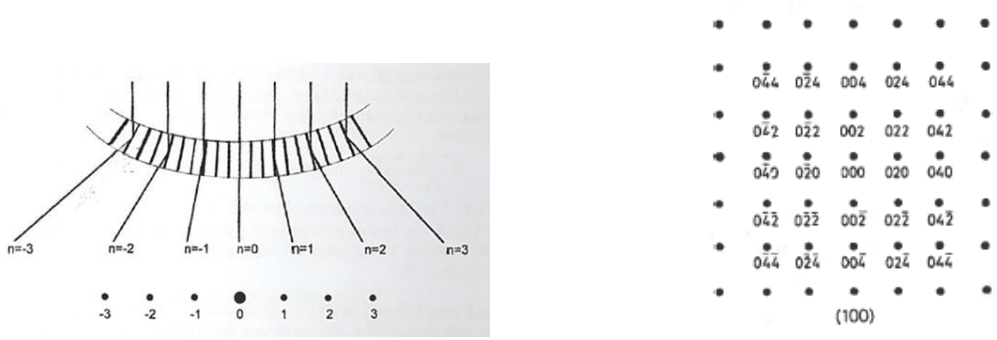

Figure 2.13: The diffraction pattern . a) The effect of sample bending on diffraction and b) A typical diffraction pattern resulting from (100) planes [45].

2.5.2 Contrast

2.5.2.1 Bright field and dark field imaging

If all the radiation that leaves the plane had been focused on the screen, the only contrast one would observe would be due to differences in absorption and scattering. To improve the contrast one may insert an aperture in the focal plane of the objective lens. This results in one of two image modes, depending on the nature of the objective aperture.

As depicted in Figure 2.14, a bright field image is formed when only the direct beam passes through, resulting in darker areas where the Bragg conditions are satisfied. However, even if the conditions in principle are satisfied for the whole area in question, the always present bend of the sample results in the majority of the area not satisfying the conditions, giving the light background.

On the other hand, using a different type of objective aperture, only the diffracted beams will be used to create an image on the fluorescent screen, creating a dark field image.[45]

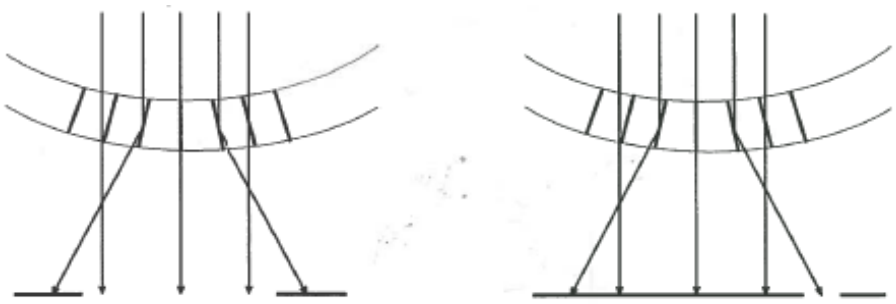

Figure 2.14: Image formation in bright field (a) and dark field (b) image mode [45].

2.5.2.2 Contrast from particles

TEM is an excellent instrument for the investigation of smaller particles and precipitates in the sample, due to the large magnification which may be obtained, and the use of diffraction. There are mainly two ways to do this, depending on the coherency or incoherency of the particle. Incoherent particles have a different crystal structure and is oriented differently than the lattice of its surrounding matrix, and will satisfy different diffraction conditions. In this case, the contrast may be obtained by tilting the sample until the angle satisfies the diffraction conditions of the particle. In this way, given the use of bright field, the particle will diffract the electron beam and be imaged darker than its surrounding matrix.[45]

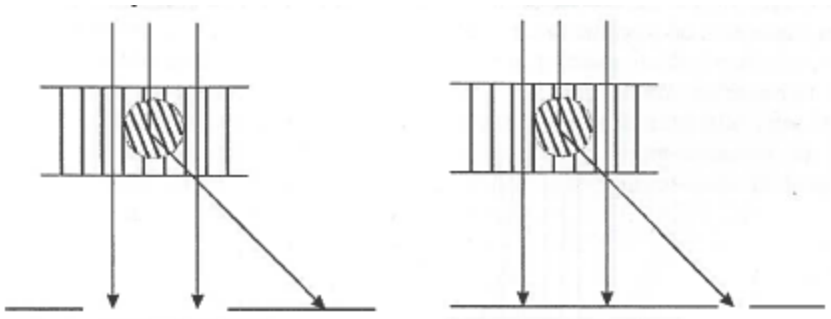

Figure 2.15: Contrast achievement of particles in bright field (a) and dark field (b) image mode [45].

In age-hardenable alloys such as Al-Mg-Si, the hardening precipitates β'' are semi-coherent with the matrix, meaning that the atomic planes of matrix and precipitate have a more or less continuous transition. This implies that the above mentioned technique may not be applied, as both matrix and particle will satisfy the same diffraction conditions. However, due to small differences in planar distances, a stress field is induced around the precipitates, resulting in local

reflections. When imaging coherent particles, the contrast is likely to originate from the stress field around the precipitates, imaged darker than its surroundings. [45]

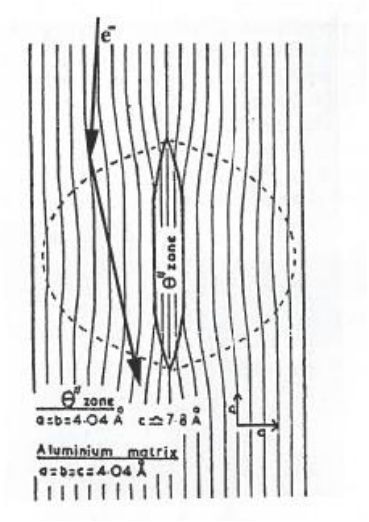

Figure 2.16: Contrast mechanism for coherent precipitates [45].

3 Experimental procedure and setup

3.1 Materials

Four Al-Mg-Si alloys with varying concentrations of silicon, iron, copper, magnesium and manganese were received as extruded round bars, and formed the basis of this thesis. The three first alloys in Table 3.1 below, 6181, KFC and 6082, contained a similar amount of Si (~1 wt%) and Mg (0.65-0.8 wt%), which is reflected by their Mg/Si ratio. KK13 contained only 0.52 wt% Si, while the Mg-content in turn was higher relative to the other alloys, resulting in an Mg/Si ratio corresponding to the Mg_2Si phase, and with excess Mg relative to the common hardening phase Mg_5Si_6 (β").

6181 and 6082 have an almost identical alloying content, except for the introduction of 0.55 wt% Mn in 6082. KFC and KK13 were the only alloys containing Cu, with 0.8 wt% and 0.4 wt% respectively, and where the former had more than twice as high an Fe-content as the other materials with 0.5 wt%.

Table 3.1: Alloys investigated in this thesis. The Mg/Si ratio of the expected hardening phase is shown in the last column.

Alloy	Si	Fe	Cu	Mg	Mn	Mg/Si	Mg_5Si_6
6181	0.95	0.22	-	0.75	-	0.79	0.83
KFC	1.00	0.50	0.80	0.80	-	0.80	
6082	1.00	0.20	-	0.66	0.55	0.66	
KK13	0.52	0.21	0.40	1.01	0.55	1.94	

3.2 Hardness testing and determination of electrical conductivity

Hardness tests were performed to determine the ageing time necessary to reach peak hardness in each alloy. Slices of the extrusion bars were cut in Struers' Discotom-5 with Struers' 20A25 cut-off wheel and thereafter solution heat treated in a salt bath at 530 °C for 10 minutes, before being water quenched. After ageing naturally in room temperature for 4 hours, they were placed in an oil bath at 170 °C, and held for 0 min, 5 min, 20 min, 1 hour, 2.5 hours, 6 hours, 15 hours, 35 hours, and 75 hours, respectively. The samples were immediately water quenched after artificial ageing. To ensure a satisfactory level surface for testing, the samples were ground manually in Struers Rotor-Knuth with grinding papers 320P, 500P, 800P and finally 1200P.

The hardness tests were conducted in Matsuwa DVK-1S with 1kp load, a holding time of 15 s, and a loading speed of 100 μm/s. Five indentations were taken per sample, for which the diamond indentation diameters were measured and converted to Vickers Hardness.

For measurements of the electrical conductivity, the samples from the hardness tests were reused, except for the 0 min sample, which was solution heat treated again to avoid effects of an extended natural ageing. The measurements were performed with Foerster Sigmascope 2.069 in a closed room, to minimize air circulation and temperature differences. Prior to testing, the apparatus was first calibrated with standards having a conductivity of 58.5 MS/m and 4.415 MS/m. The frequency was set to 120 Hz and the probe had a length of 7 mm.

3.3 Tensile tests

Three tensile test specimens were prepared from each alloy, and machined into the dimensions illustrated in Figure 3.1, at Finmekanisk Verksted, NTNU. After machining, heat treatment was performed according to the findings from the hardness tests to induce peak hardness conditions, T6.

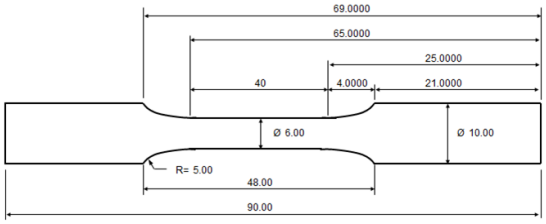

Figure 3.1: The dimensions of the tensile test specimens .

The testing was performed at SINTEF's laboratory in Perleporten, NTNU. A laser extensometer was used with the tensile test instrument Instron 100 kN at a nominal strain rate of 1.2 mm/min. When necking initiated, the lasers were continuously moved around the neck to ensure that the region with the smallest cross-section was measured. The data from the tensile tests, recieved in true stress and true strain, was adjusted by Bridgman correction, as explained in 2.3.1 Stress strain curves.

An additional set of tensile tests were performed to compare the effect of work hardening in 6082 and KK13 as-extruded, with its aged counterparts. First, three parallels of each alloy were tested in the laser extensometer and compared to the results from the aged specimens. The

results indicated that a pre-straining of 8.2% would be beneficial to obtain a desired basis of comparison between the aged and the as-extruded specimens.

Six new parallels of 6082 and KK13 were machined and pre-strained to 8.2% in MTS-810 100kN at Department of Materials Technology and Engineering, NTNU. Out of these, three parallels of each alloy were tested directly in Instron 100kN with a laser extensometer after resting for one week, while the three remaining specimens were aged for a time corresponding to peak hardness conditions prior to testing. The latter rested for six days before ageing was initialized, and were tested on day 7.

3.4 Microscopy and sample preparations

3.4.1 Light optical microscopy and microstructure characterization

Slices were cut from the extrusion bars in Struers' Discotom-5, as for the hardness tests, but these slices were also cut in half across the center of the cross-section. This was done to obtain images of the RD-ED plane, corresponding to the radial and extrusion direction respectively, and displayed in Figure 3.2.

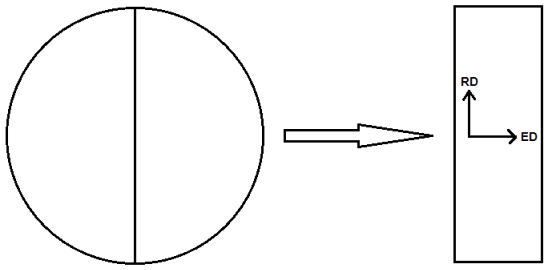

Figure 3.2: Illustration of the microscopy sample geometry and directions.

After solution heat treatment in a salt bath at 530°C, and water quenching, the samples were cold mounted in Struers Clarocit solution. Thereafter, they were ground in the same manner as the samples for the hardness tests, but with two additional grinding steps, using Struers' grinding paper 2000P and 4000P. Polishing with a fabric with diamond spray of grain sizes down to 6, 3 and 1 μm was executed with Struers' TegraPol-31, and finally they were anodized in an HBF_4 solution for 90 seconds. The power supply, TTi QL355, was set to 20 V.

After anodizing, the microstructure of the alloys were investigated in Leica MEF4M. To achieve a satisfactory contrast the polarizer was set to the crossed position and a sub-parallel γ-

plate was inserted. The γ-plate was manipulated manually until the desired contrast was achieved. The images used in this thesis were taken with a magnification of 25X.

3.4.2 Scanning electron microscopy

All the samples prepared for SEM microscopy, except the ones used for fracture surface inspection, were prepared as for the light optical microscopy samples, bar the anodizing step. Any additional steps executed for the different analyses will be presented in the following sub-chapters.

Different investigations and operation modes in SEM require different settings to obtain optimal results. The settings applied in this thesis are specified in Table 3.2 below.

Table 3.2: The settings used for the different SEM investigations.

Setting	Particle analysis	Chemical analysis	Grain sizes	Fractography
Operation mode	BSE	EDS	EBSD	SE
Acceleration voltage	15 kV	20 kV	20 kV	20 kV
Working distance	15 mm	12.5 mm	ca 23 mm	10-30 mm
Current mode	High current	High current	High current	High current
Aperture diameter	60 µm	120 µm	300 µm	30 µm
Tilting angle	0°	0°	70°	0°

3.4.2.1 Primary particle investigation

To investigate the primary particle distribution, samples identical to the ones employed in the light optical microscope were produced. Except for the anodizing step, the rest of the preparation was identical to what was performed on the above mentioned samples.

The particle analysis in Zeiss Ultra 55 Limited Edition was conducted using backscatter electrons to get a Z-contrast which would separate the iron-based particles, with a higher mean atomic number, from the aluminum matrix. The settings used for the particle analysis are shown in Table 3.2 above. Three images of each alloy were taken at a magnification of 250X.

The images for the particle analysis required further treatment in an image processing software. The software used was a freeware called ImageJ, where the images were loaded and processed. First the images were converted to 8-bit, before they were sharpened using an automatic setting in the software. The background was then substracted, before the color threshold was adjusted manually to give as precise a representation of the particle size and distribution as possible. The last step was done by visually comparing the manipulated image with the original.

The resulting data from ImageJ was given further treatment in Excel, to find averages of the particle distribution and characteristics between the three images of each alloy. To achieve an intuitive representation of the particle size, the area of each particle was converted to the Equivalent Circle Diameter (ECD) through the following equation

$$ECD = \sqrt{\frac{4}{\pi} \cdot A} \qquad 20$$

where A is the area of a given particle [46]. The ECD was also chosen as it would make it easier to obtain a basis of comparison with the Feret diameter, which was calculated automatically by the software. The Feret diameter represents the largest distance between two points in the particle, and by comparing it with the ECD, one would get an idea of the particle shape. An illustration of the Feret diameter is provided in Figure 3.3.[47]

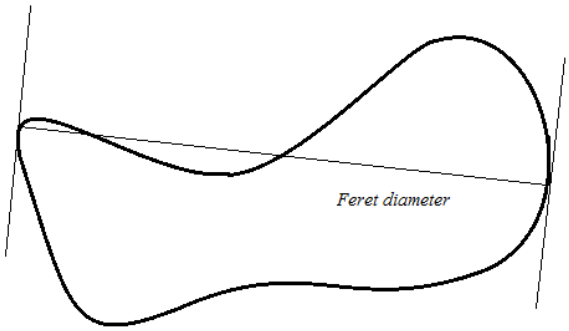

Figure 3.3: An illustration of the Feret diameter.

3.4.2.2 Chemical analysis (EDS)

For the chemical analysis, an additional polishing step was applied on the samples from the primary particle investigation. They were chemically polished with an OP-S suspension solution with an MD Chem polishing plate for 2 minutes, in an attempt to separate them from the matrix and thus ensure superior signals with less noise from the surroundings. Prior to inserting them in the SEM, they were placed in plasma cleaner Fishione Instruments' Model 1020 for 6 minutes to remove contaminations, such as carbon, from the surface.

While operating the SEM, random particles were selected and analyzed in each alloy, using the settings mentioned in Table 3.2. To obtain a satisfactory signal an aperture of 120 µm was employed, even though this increases the area, or volume, analyzed.

3.4.2.3 Fracture surface characterization

Due to the limited possibilities and necessity to clean the fracture surfaces, the specimens were merely rinsed in ethanol, before being placed in the plasma cleaner Fishione Instruments' Model 1020 for 6 minutes prior to SEM investigation.

The small aperture size of 30 µm along with the large working distance of 30 mm were used to achieve a desired depth of field in the low magnification images. While increasing the magnification, the working distance was reduced to 10-15 mm to obtain a superior resolution.

3.4.2.4 Grain size detection through EBSD

In addition to the sample preparation scheme mentioned in the introduction to this section, EBSD samples of aluminum require electro-polishing to attain good diffraction patterns for the calibration of the indexing process. For 6181 and KFC this was performed in Struers Lectropol-5, using an A2 electrolyte kept at -25°C. The contents of A2 are shown in Table 3.3 below.

Table 3.3: The composition of electrolyte A2.

Substance	Amount
Percloric acid	78 ml
Water	120 ml
Ethanol	700 ml
Butycellosolve	100 ml

EBSD scanning is sensitive to irregularities in the samples surface and thus plasma cleaning in Fishione Instruments' Model 1020 was required to ensure adequate precision. As with the former samples, they were held for 6 minutes each.

3.4.3 Transmission electron microscopy

The name Transmission Electron Microscope suggests that the electron beam is required to pass, or transmit, through the sample. This implies a certain limitation with respect to the sample thickness. The maximum sample thickness is commonly defined to be 100 nm, but depends on the specific material at hand [48].

To obtain the desired thickess, a slice of each alloy was cut as thin as possible with Struers Accutom-5, using Struers 10S25 cut-off wheel at a speed of 0.04 mm/s. After this, the slice was attached with double sided tape to a piece of plexiglass, and ground with Struers grinding paper P120, P500, P1200 and P2000. The sample was turned and reattached to the plexiglass to

achieve the same surface quality on both sides. Grinding was stopped when the edge of the slice was no longer felt when sliding a finger across the plexiglass.

Subsequent to grinding, the plexiglass was inserted into a container of liquid nitrogen to ensure a means of removal that would strain the thin slice to a minimal degree. After a couple of minutes the plexiglass was removed from the container, and the tape attaching the thin slice was cut. To remove remains of the tape the slice was now placed in acetone. The sample was cleaned with a piece of cotton and dried on filter paper. Finally, TEM disks of 3 mm in diameter were punched out with Gatan 659 Disc Punch.

To attain the satisfactory thickness the discs were electropolished in Struers Tenupol-5 with an electrolyte consisting of 1/3 HNO_3 and 2/3 methanol. The settings employed are defined in Table 3.4.

Table 3.4: Settings in Struers Tenupol-5 used for electropolishing TEM specimens.

Setting	Value
Voltage	20 V
Temperature	-25 °C
Polishing time	No limit
Light step	20
Graphic time scale	Auto
Flow mode	Single flow
Pump flow	25

3.4.3.1 Precipitate imaging

Precipitation was expected to occur in the form of needles along <100> in all alloys involved [27]. To obtain images for their characterization a given grain must be tilted in such a way that two <100>-directions are perpendicular to the electron beam.

This was achieved by utilizing a small objective aperture, and moving around the sample identifying darker areas, indicating a higher level of diffraction, corresponding to lower zone axes. When finding a suitable area/grain, the sample was tilted until the commonly observed (100) diffraction pattern illustrated in section 2.5.1 was observed. In the same section, Bragg's law was introduced, and it follows from this phenomenon that there will exist an angle between the incoming electron beam and the (100) planes when the (100) diffraction pattern is achieved. However, this angle is of such a small magnitude that it does not affect the precipitate characteristics to any significant degree ($\lambda << d$ in Eq. 19).

3.4.3.2 Grain boundary and PFZ inspection

To obtain the best possible conditions for observing the grain boundary particles and precipitation free zone, it was attempted to tilt the specimen until the grain boundary was parallel with the electron beam. When this was achieved, the grain boundary could be observed at minimum width, and jagged, according to the existing disorder. Tilting in this way would also ensure a more reliable characterization of the precipitation free zone.

4 Results

4.1 Ageing

To obtain a satisfactory presentation of the ageing behavior, the hardness values were plotted against the holding times. It was also of interest to get an additional view on the ageing rate, which was achieved by plotting the electrical conductivity of the same samples, against the holding times.

4.1.1 Ageing behavior

The ageing curves shown in Figure 4.1 were found to be consistent with each other, although KFC required 35 hours (2100 min) to reach peak hardness, compared to the 15 hours (900 min) required for the other three alloys. The two Cu-containing alloys, KFC and KK13, showed a more rapid ageing behavior in the initial stages, where 6181 and 6082 had only a moderate increase in hardness until passing 1 hour. After this point, the excess-Si alloys increased more rapidly than KK13. KFC was the only alloy to stand out in terms of peak hardness value, with 163 ± 2.8 HV1. The other three alloys all peaked in the region 120-135 HV1. The peak hardness values are displayed in Table 4.1 below. Based on these finding, the ageing times to peak hardness throughout this thesis were chosen to be 35 hours for KFC, and 15 hours for the three other alloys.

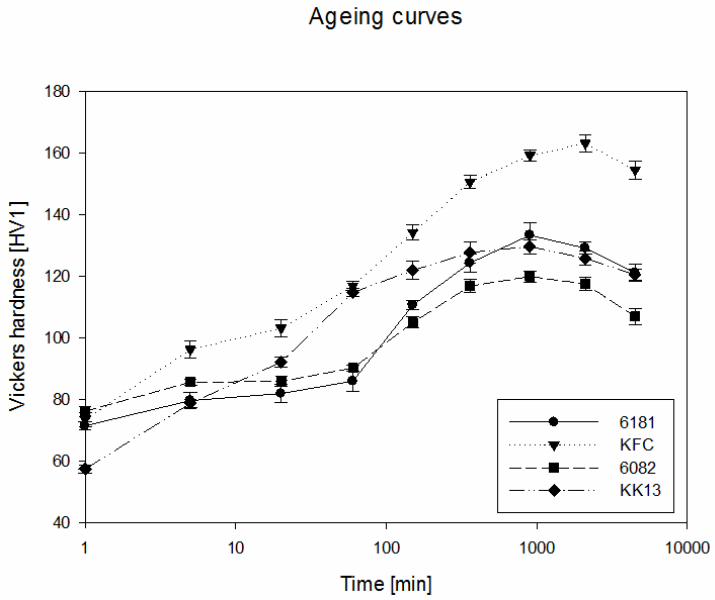

Figure 4.1: Hardening behavior.

Table 4.1: Peak hardness values.

Alloy	Vickers hardness [HV1]
6181	133.3 ± 4.1
KFC	163.1 ± 2.8
6082	119.9 ± 1.9
KK13	129.6 ± 2.3

4.1.2 Electrical conductivity evolution

The electrical conductivity of the samples from the hardness tests was measured, and is illustrated in Figure 4.2. The results obtained from the 0 min samples are assumed to be unrepresentative, due to contamination of the samples or other possible effects, and their relatively large value will be ignored in the rest of this thesis.

In terms of electrical conductivity, the alloys are ordered more or less according to their alloying content. The least alloyed of the materials, 6181, consequently displayed the largest electrical conductivity. The three excess-Si alloys exhibited a rapid increase after 1-2.5 hours had passed, which correlates with the ageing curves. After this point, 6082 increased in almost exactly the same manner as 6181, while the two Cu-containing alloys had a lower increase in conductivity. KK13 displayed an almost linear increase during the entire ageing scheme, while the other Cu-containing alloy (with excess-Si), KFC, increased more rapidly between 1 and 15 hours, and thereafter developed more or less in parallel with the KK13 graph. Neither KK13 nor KFC replicated the rapid increase found in the early stages of the ageing curves.

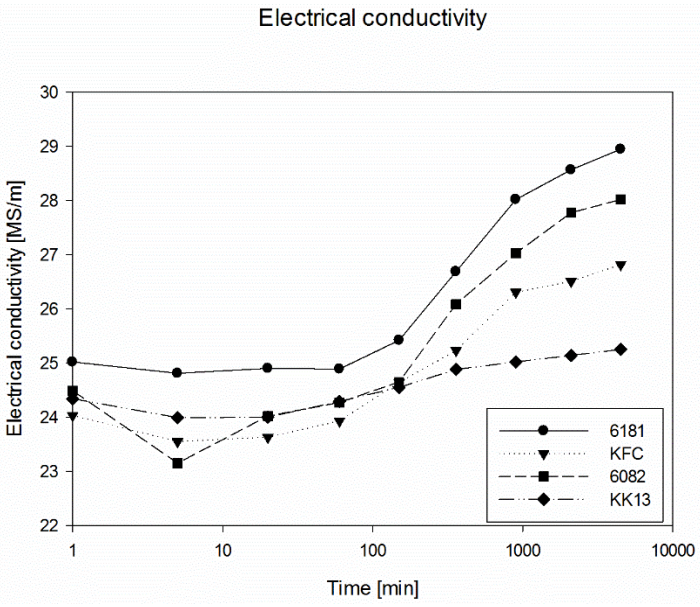

Figure 4.2: The electrical conductivity evolution during ageing.

4.2 Tensile tests

The graphs presented in this section are all shown in terms of true stress and strain. After initiation of necking, the curves have been adjusted with Bridgman correction, but the non-treated graphs are also plotted (in black), where their point of separation identifies neck initiation.

4.2.1 Aged specimens

The tensile tests aged to T6, and displayed in Figure 4.3, revealed interesting contrasts to the ageing curves. While KFC showed the highest peak hardness value, it was KK13 which displayed the highest tensile strength, with 465 MPa. The Mn-containing alloys seemed to have a more superior behavior in tension than 6181 and KFC, relative to the hardness tests. While KK13 performed superior in terms of stress, it also displayed the second best ductility with an elongation of 64.6% to fracture. 6082 was the weakest of the alloys in the hardness tests, but performed better in the tensile test compared to 6181, with its tensile strength being 29 MPa higher. It also displayed the best ductility of all the alloys by far, with an elongation to fracture of 79.2%.

The 6181 alloy went to fracture at the lowest strain, of 23.1% elongation, and also showed the lowest tensile strength with 358 MPa. In comparison, KFC displayed a significantly higher tensile strength than 6181, which was to be expected from the hardness tests, but also a notably larger strain at fracture with an elongation of 42.9%.

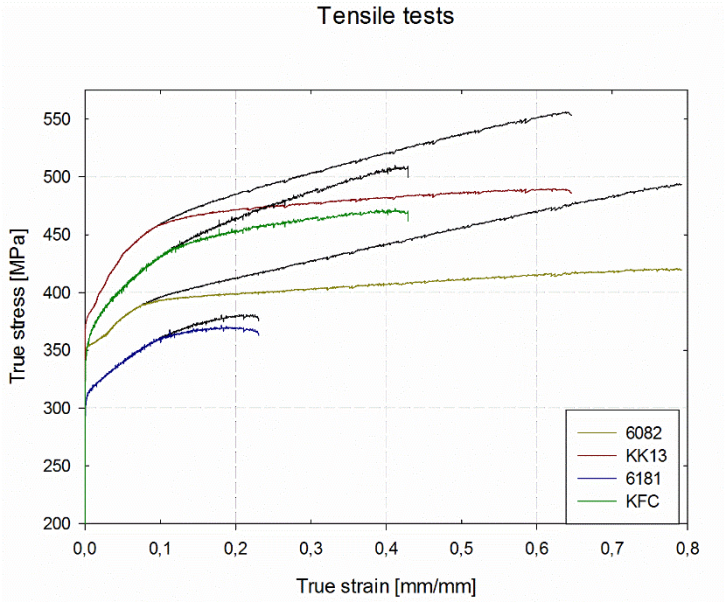

Figure 4.3: Stress-strain curves in temper T6, calculated with Bridgman correction. The black curves represent each alloys non-corrected curve, indicating the initiation of necking in the point in which they separate.

Table 4.2 below quantifies the results from the tensile tests. 6181 yielded at the lowest stress with 307 MPa, and also had the second highest strain at necking, though the lowest strain at fracture. As mentioned above, 6082 had the highest strain at fracture, but also the lowest strain at neck initiation, going to necking with an elongation of 7.4%. Both of the Cu-containing alloys showed an impressive strength/ductility relationship with tensile strengths of 434 MPa for KFC and 456 MPa for KK13, and with elongations to fracture of 42.9% and 64.6%, respectively.

Table 4.2: Values extracted from the tensile tests. All values are given in terms of true stress and strain. Peak true stress is the maximum stress achieved prior to fracture, adjusted with Bridgman correction.

Alloy	Yield strength [MPa]	Tensile strength [MPa]	Strain at max. load [mm/mm]	Peak true stress [MPa]	True strain at fracture [mm/mm]
6181	307	358	0.096	372	0.231
KFC	347	434	0.112	473	0.429
6082	353	387	0.074	421	0.792
KK13	376	456	0.095	490	0.646

4.2.2 Aged vs. non-aged specimens

Additional tensile tests were performed on the two Mn-containing alloys 6082 and KK13 to investigate their behavior without additional heat treatment after extrusion, that is, in temper T5. The results are shown in Figure 4.4 and suggest that a yield strength, similar to the ones

after ageing, could be achieved by straining the tensile samples by 8.2% prior to testing in the laser extensometer. The observation was based on the similar work hardening exhibited by the alloys, indicated by their parallel graphs after necking. This implied that straining prior to tensile testing would merely shift the graphs of the non-heat treated alloys to the left, eventually ending up with a very similar result. With an elongation to necking of 14.7% for non-aged 6082 and 14.8% for non-aged KK13, the ductility was not expected to suffer dramatically compared to the aged samples, with an expected result of 6.4% in strain at necking for the pre-strained specimens of both alloys.

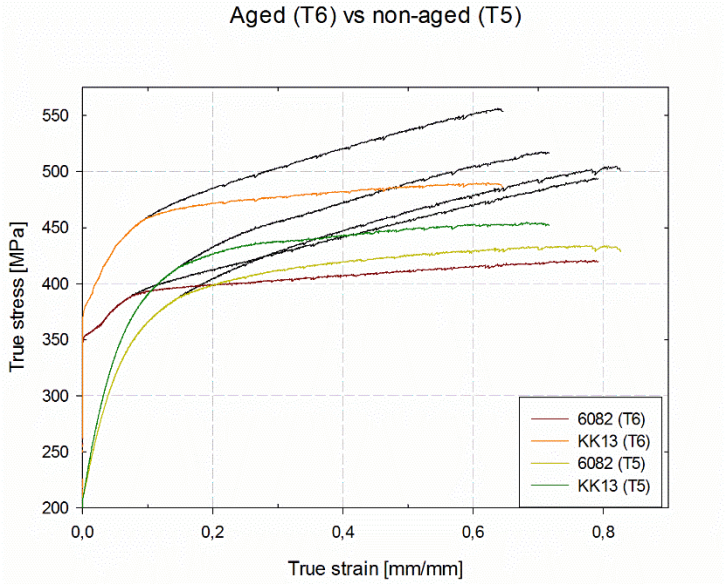

Figure 4.4: Stress-strain curves comparing aged (T6) alloys with non-aged (T5).

Table 4.3 below shows the expected poor yield strength of the non-aged alloys at just above 200MPa, compared to 353 MPa and 376 MPa of aged 6082 and KK13, respectively. However, the tensile strength of 6082 was identical in both states, and also close in value for KK13, implying a rapid work hardening. The peak true stress was in fact higher for the non-aged 6082, and closer in value for the aged and non-aged KK13 specimens compared to their gap in tensile strength.

Table 4.3: Important values extracted from the tensile tests of non-aged specimens, compared to T6.

Alloy	Yield strength [MPa]	Tensile strength [MPa]	Strain at max. load [mm/mm]	Peak true stress [MPa]	True strain at fracture [mm/mm]
6082 (T6)	353	387	0.074	387	0.792
6082 (T5)	213	386	0.147	440	0.827
KK13 (T6)	376	456	0.095	479	0.646
KK13 (T5)	213	413	0.148	462	0.717

4.2.3 Pre-strained specimens

The stress-strain curves for the pre-strained specimens of 6082 (Figure 4.5) proved to obtain a quite similar shape as compared to the T6 curves. In fact, the results indicated a stronger work hardening for the pre-strained specimens as compared to the T6 specimens, which was also suggested in Figure 4.4. However, it also seems to have resulted in over-ageing of the specimens which were artificially aged after pre-straining. They displayed a vastly inferior strength, but had a ductility just slightly superior to the non-aged specimens. In fact, all specimens showed the same level of ductility regardless of strength.

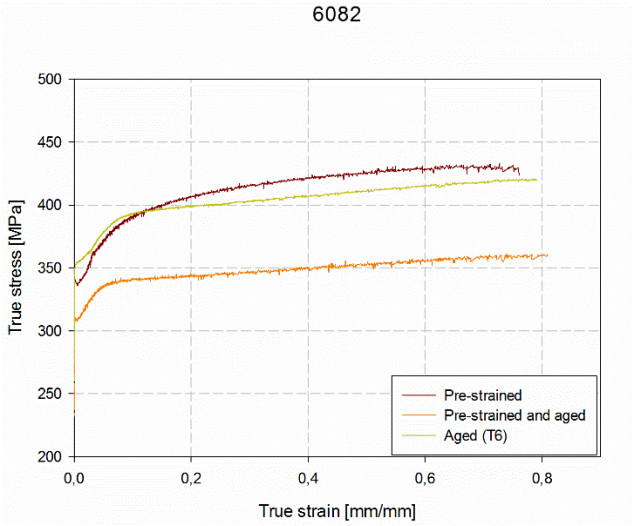

Figure 4.5: The stress-strain curves of 6082 as pre-strained from T5, pre-strained and aged, and only aged to T6.

Table 4.4 shows the most important material properties extracted from these tensile tests. Interestingly, the pre-strained sample, subjected to natural ageing for approximately one year, displays the same tensile strength as the T6 sample at 385-7 MPa, while displaying a superior elongation to necking at 8.4% compared to 7.4% for T6. However, the yield strength as pre-strained (338 Mpa) was slightly lower in comparison with T6 (353 Mpa). This was also the case

for the specimens which had been aged after pre-straining, showing poorer results for all properties, except true strain at fracture.

Table 4.4: Pre-strained 6082 specimens. Important values extracted from the tensile tests of 6082 specimens that had been pre-strained from T5, pre-strained from T5 and aged, and aged to T6.

Name	Yield strength [MPa]	Tensile strength [MPa]	Strain at max. load [mm/mm]	Peak true stress [MPa]	True strain at fracture [mm/mm]
6082 (pre-strained)	338	385	0.084	430	0.762
6082 (pre+aged)	307	335	0.052	361	0.810
6082 (T6))	353	387	0.074	421	0.792

The results from the KK13 curves in Figure 4.6 displayed a different behavior for the pre-strained and pre-strained and aged specimens. The ageing of the pre-strained sample seems to have had a beneficial effect on strength, showing the same yield strength as the T6 samples, but a much inferior work hardening with respects to the T6 samples. As for the 6082 specimens, the pre-strained samples showed a slightly lower yield strength than for T6. The ductility was similar in all states, with the pre-strained and aged specimens showing a slightly larger elongation to fracture.

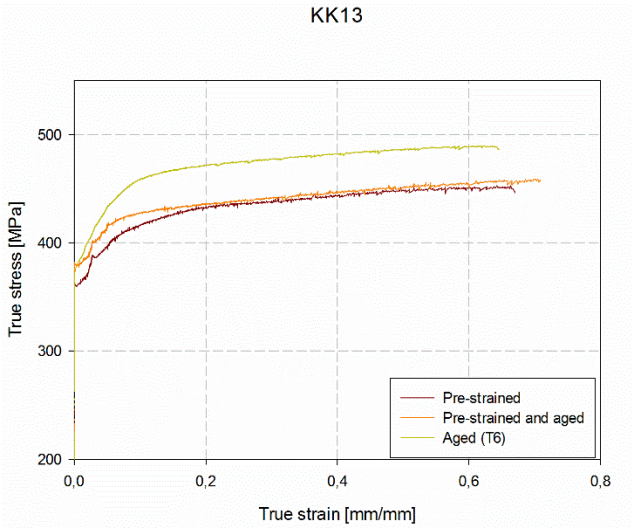

Figure 4.6: The stress-strain curves of KK13 as pre-strained from T5, pre-strained and aged, and only aged to T6.

The results in Table 4.5 further suggests a beneficial effect of ageing after pre-straining with respects to the strength, although the elongation to necking has been reduced. It is obvious though, that the T6 sample has better properties on most points, having an elongation to necking of 2-3% more than for the other two states. Its ductility is somewhat lower at 64.6% elongation,

but its tensile strength and peak true stress was ~35-40 MPa larger than for the specimens in the two other states.

Table 4.5: Pre-strained KK13 specimens. Important values extracted from the tensile tests of KK13 specimens that had been pre-strained from T5, pre-strained and aged, and aged to T6.

Name	Yield strength [MPa]	Tensile strength [MPa]	Strain at max. load [mm/mm]	Peak true stress [MPa]	True strain at fracture [mm/mm]
KK13 (pre-strained)	359	409	0.077	452	0.670
KK13 (pre+aged)	378	420	0.066	459	0.709
KK13 (T6)	376	456	0.095	490	0.646

4.3 Constituent analysis

The constituents were analyzed in SEM to investigate their spatial distribution, size, shape, and composition. Electron backscatter imaging was employed to achieve a satisfactory contrast for the constituent distribution images, while EDS was used to find the chemical composition of the particles.

4.3.1 Constituent distribution

By visual inspection of the images in Figure 4.7 it seemed evident that 6181 contained the fewest constituents, while the other three images are more difficult to tell apart. However, all alloys seemed to contain elongated constituents aligned in the direction of extrusion, which was to be expected from the nature of the extrusion process. In addition, one could observe that the particles were not homogenously dispersed, as some areas seemed to contain a higher density of particles than others.

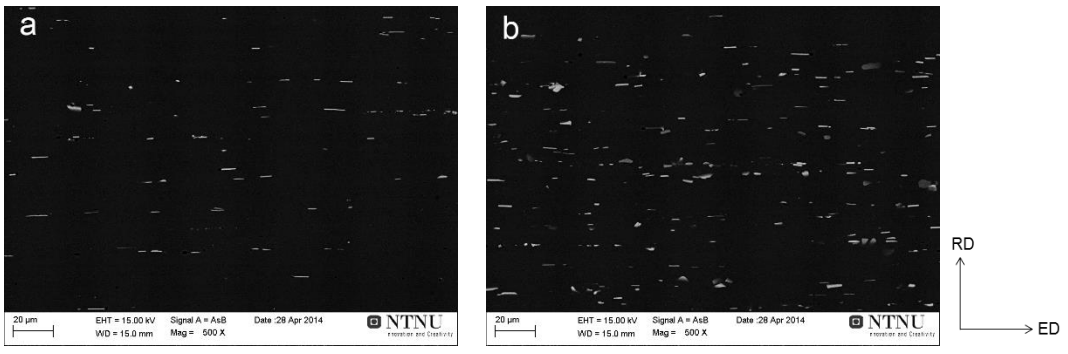

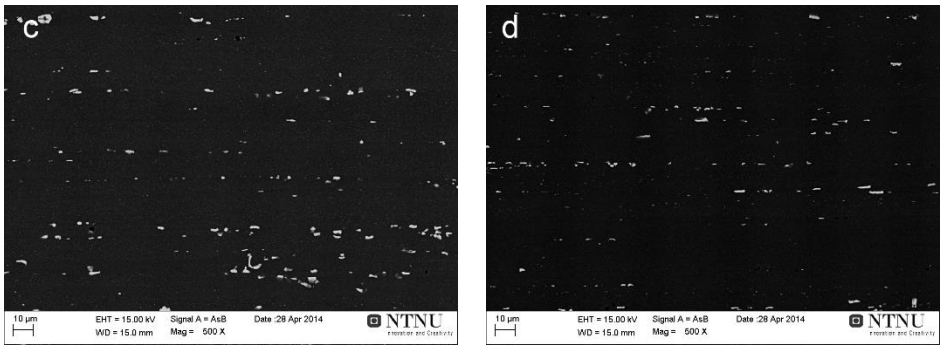

Figure 4.7: SEM images of constituents in 6181 (a), KFC (b), 6082 (c), and KK13 (d), at 500X magnification.

The result of the analysis of the primary particle size distribution in ImageJ is shown in Figure 4.8. 6082 and KK13 contained a larger number of smaller particles than what was the case for 6181 and KFC. Additionally, less coarse particles were found in the KK13 alloy, where the largest particles had a spherical diameter of 4.5 µm. Constituents with a spherical diameter of 6 µm were observed in 6181 and 6082, while the largest constituents in KFC had a size of 6.5 µm. It must be stressed however, that not all three images of each alloy contained some of the larger constituents, resulting in the vast standard deviation seen for the feret diameter in Figure 4.8.

The most observed constituents in 6181 and KFC had ECDs between 1 and 1.5 µm, while constituents between 0.5 and 1 µm were the most common in the Mn-containing alloys. The feret diameter was, for all alloys, approximately twice as large as their respective ECDs in each interval, giving evidence of highly elongated particle shapes.

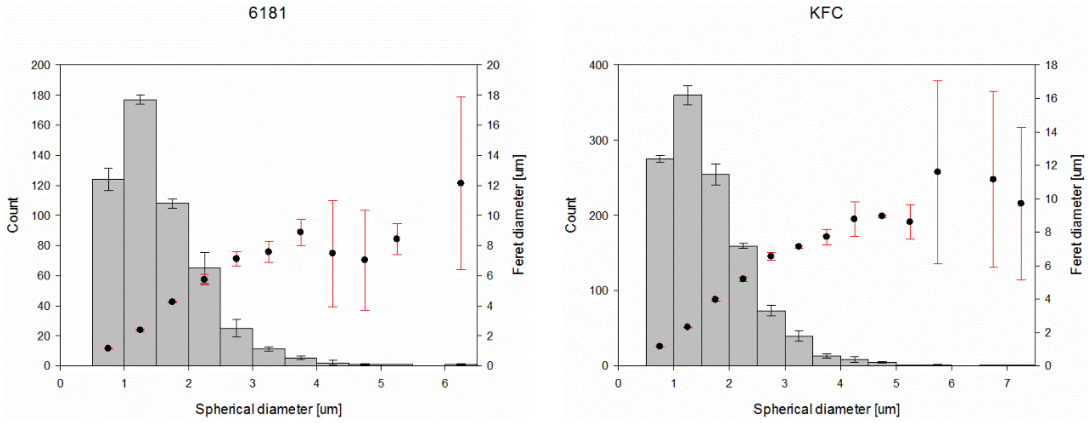

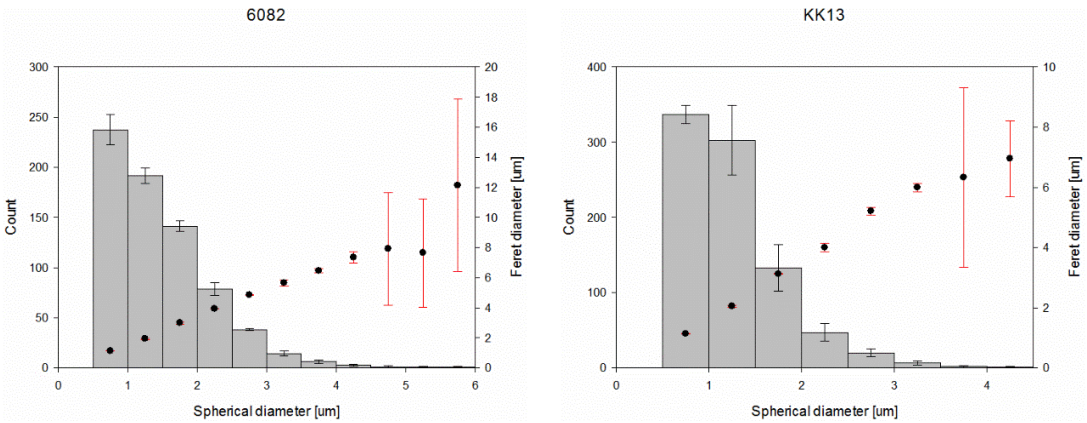

Figure 4.8: Particle distribution charts. Grey bars indicate the number of particles in each size interval, while black dots indicate the corresponding average feret diameter. Note: The analysis was taken from images at 250X to ensure sufficient statistics. These may be found in 0.

From Table 4.6 one can see average values from the analysis. The iron-rich KFC alloy contained by far the most primary particles with more than twice the amount found in 6181. It also contained the largest average constituent size at 1.764 ± 0.029 µm. This is not too surprising seeing that it contained 0.5% Fe compared to around 0.2% Fe in the other three alloys. There were no significant differences between the other alloys, though it is noticeable how the Si-depleted KK13 alloy had a lower average constituent size than 6082, while they also covered a smaller fraction of the total area.

6181 was the alloy with the lowest total alloying content, and had the lowest number of particles, covering the smallest area. It should be noted however, that its average particle size was only slightly lower than what was the case for KFC.

Table 4.6: Result from the particle distribution analysis.

	6181	KFC	6082	KK13
Number of particles	519 ± 19	1192 ± 25	712 ± 31	849 ± 94
ECD [µm]	1.647 ± 0.060	1.764 ± 0.029	1.593 ± 0.015	1.314 ± 0.060
%Area	0.796 ± 0.083	2.090 ± 0.055	1.019 ± 0.046	0.836 ± 0.161
Feret [µm]	3.325 ± 0.097	3.359 ± 0.036	2.405 ± 0.037	2.074 ± 0.121

4.3.2 Chemical analysis

The results from the EDS analysis may not be taken too literally as the analyzed volume is likely to reach beyond the particle and bring in signals from the matrix. However, ignoring the exact concentration of each element, evaluations may be made as to the type of primary particles

involved by comparing their relative differences. Comparing the concentration of Mg in the particles of all alloys in Figure 4.9, with its corresponding point analysis from the matrix, indicated that Mg was not involved in the composition of any of the constituents. The same applies for Cu in KFC, which showed more or less similar values in the particles and the matrix. In KK13 however, Cu seemed to be present in the constituents as its Cu peaks were consistently higher for these, as compared to their corresponding surroundings.

Although the results were somewhat ambiguous, the composition of some of the 6181 constituents seemed to correspond to a β-Al_5FeSi phase (particle 2, 3 and 7) and an α-$Al_{12}Fe_3Si$ phase (particle 1, 5 and 8). Taking the case of the β-Al_5FeSi phase, and assuming some noise from the matrix in the particle spot analysis, it makes sense that the Fe content is slightly lower relative to the Si-content as the matrix contains some Si, but no observed iron. As for the α-$Al_{12}Fe_3Si$ phase, it could also be assumed that the signal has been diluted by additional signal from the matrix, returning a higher Si signal compared to Fe, than what is actually present in the particle.

KFC, having a higher Fe content than 6181, seemed to contain a similar amount of the α-(particle 2,3 and 8) and β-phase (particle 1,5 and 7). The other particles are more difficult to place, and could correspond to any of the above-mentioned phases, or others.

The constituents in 6082 and KK13 clearly include Mn in addition to Fe and Si for all particles. As mentioned in section 2.2.2.1, the literature suggests the presence of Al_9Mn_3Si, $Al_5FeMnSi$, $Al_8(FeMn)_2Si$ and α-$Al_{15}(FeMn)_3Si$, for aluminum alloys of the same composition. It is reasonable to assume that Al_9Mn_3Si is not the corresponding phase for any of the constituents analyzed as they all clearly contain Fe. In 6082, if one again assumes a large quantity of the matrix has been included in the spot analysis of the constituent, $Al_5FeMnSi$, $Al_8(FeMn)_2Si$ or α-$Al_{15}(FeMn)_3Si$ could be the corresponding phases, but the results did not yield a sufficient precision to draw any conclusions. This is also the case for KK13, although here Cu seems to be involved in all cases, with a significantly higher value than what is the case in the matrix. The Mn peaks were also lower than the Fe peaks for the constituents in this alloy, which suggests that other phases may be present.

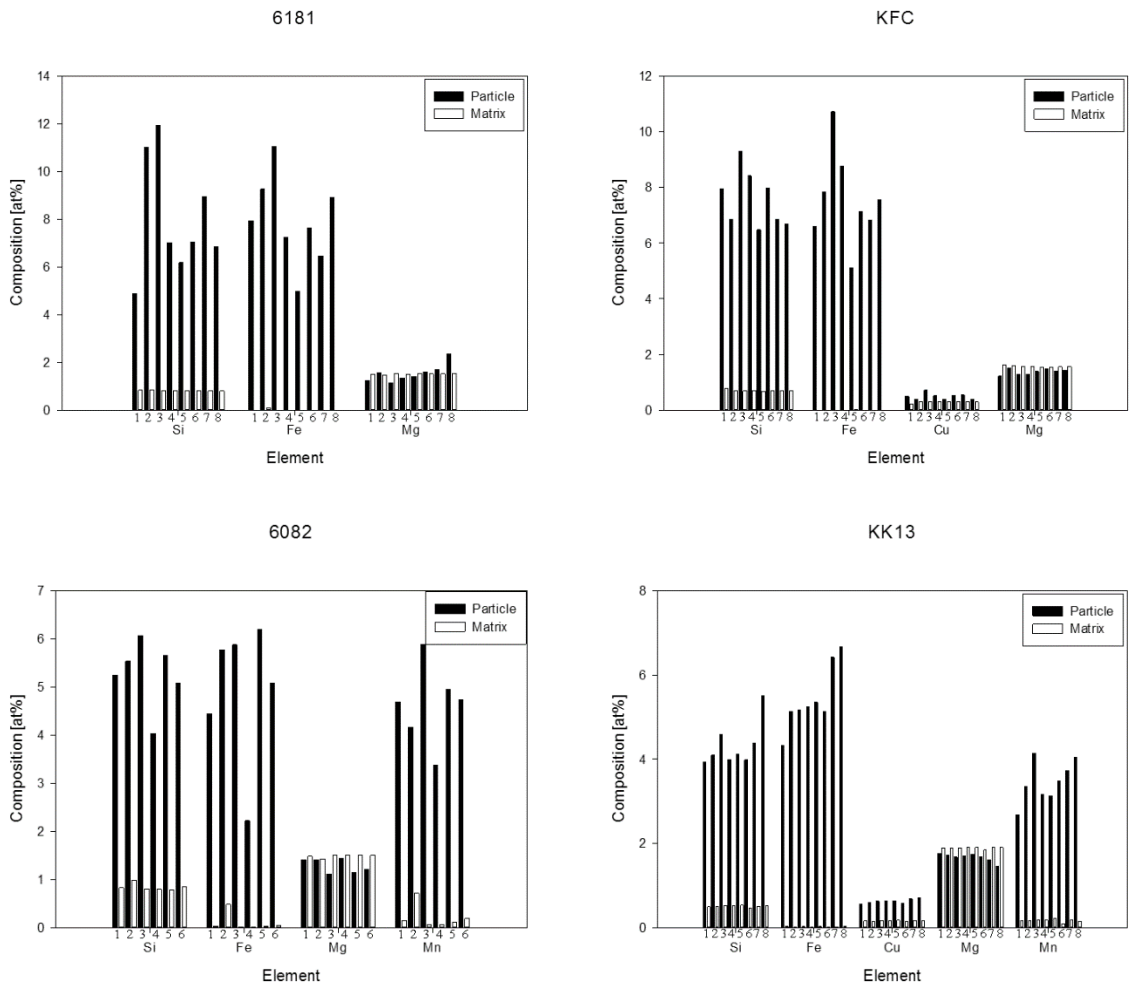

Figure 4.9: Plot of the chemical composition of a selection of constituents. The bars in the figure are pairs, with the two bars most to the left representing particle 1, its neighboring pair to the right particle 2, and so on. Aluminum balances the particle composition. Images of the particles and their respective composition may be found in 0.

4.4 Grain structure

Light microscope imaging revealed a fibrous microstructure for the two Mn-containing alloys, while 6181 and KFC were completely recrystallized after extrusion. The grain sizes of the latter two were estimated to be 67.2 ± 62.7 and 75.9 ± 64.7 µm respectively, with the large standard deviation indicating a vastly inhomogeneous microstructure. The microstructures are shown in Figure 4.10 below. 6082 and KK13 contained much smaller (sub-)grains in comparison with an average of 4.6 ± 5.7 and 4.4 ± 7.1, respectively.

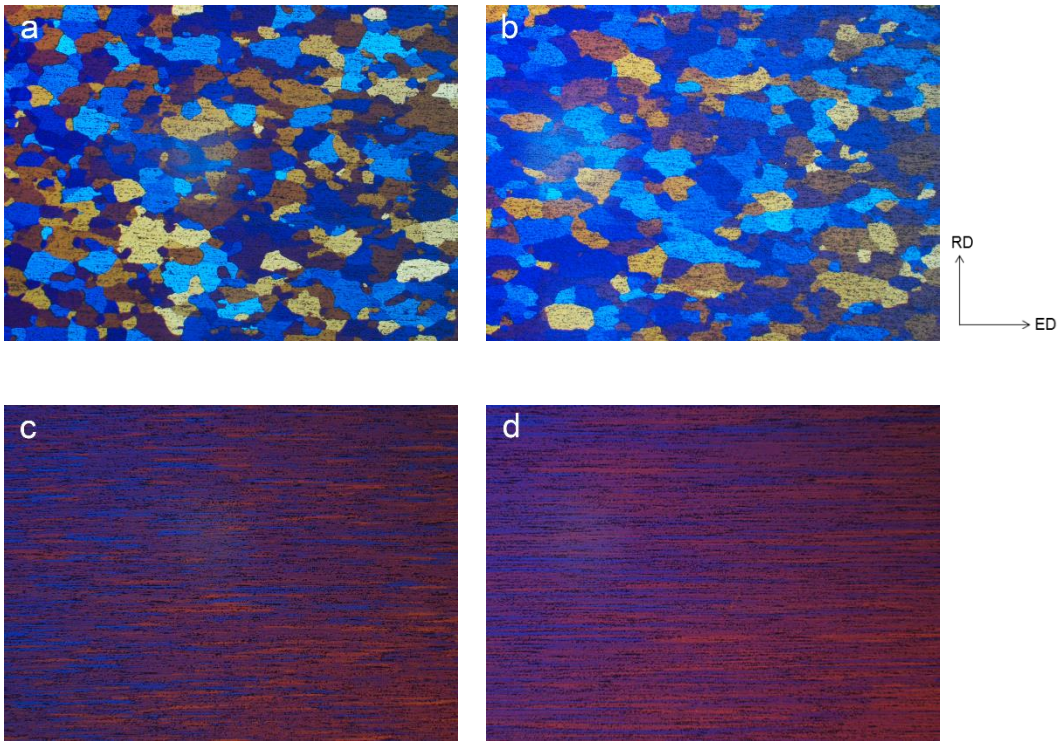

Figure 4.10: Light microscope images of the grain structure. 6181 (a) and KFC (b) were fully recrystallized, while the two Mn-containing alloys 6082 (c) and KK13 (d) display a fibrous microstructure.

4.5 Fracture surface characterization

The fracture surfaces were imaged in SEM, and by visual inspection in Figure 4.11 one can see a clear correlation between the ductility shown in the stress-strain curves and the decrease in surface area. In 6181, a decrease in surface area is hardly visible, while for KFC it has become pronounced. The two fibrous alloys displayed a vastly superior behavior in terms of ductility than the above mentioned, and thus exhibit an even larger decrease in surface area. An additional interesting factor is the way these two alloys seem to have been deformed, i.e. in such a way that a spiral has been formed inside, the more conspicuous case being that of KK13.

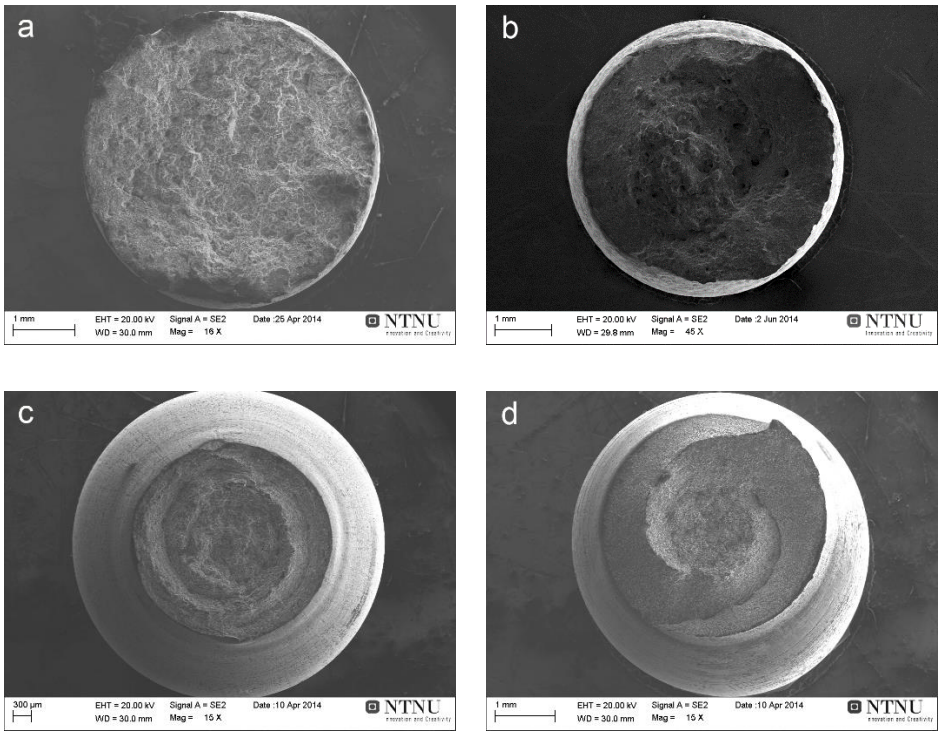

Figure 4.11: Fracture surface images of 6181 (a), KFC (b), 6082 (c) and KK13 (d).

The decrease in surface area was measured from the SEM images, and compared to the last diameter registered by the laser extensometer. The former measurements proved to deviate considerably from the latter, consistently being 10-30% lower. The results are shown in Table 4.7. 6082 and KK13 showed the largest deviation from the fracture diameter registered by the laser extensometer, indicating that this may be related to the total decrease in diameter. However, no such correlation was seen while comparing 6181 and KFC.

Table 4.7: Fracture area diameter calculated from SEM images, compared with the fracture diameter registered by the laser extensometer.

	d_{SEM} [mm]	d_{laser} [mm]	d_{SEM}/d_{laser}
6181	4.68	5.24	0.89
KFC	4.28	4.74	0.90
6082	2.92	4.07	0.72
KK13	3.55	4.29	0.83

Going higher up in magnification in Figure 4.12, there was a notable difference in dimple fraction between 6181 and KFC, which was to be expected from the stress-strain curves. The more ductile Cu-containing KFC alloy had fewer facets, while these were more prominent in

the more brittle 6181 alloy. In the case of 6082 and KK13, they both showed a highly ductile behavior, and the lack of visible facets surely give indications of a purely ductile fracture mechanism.

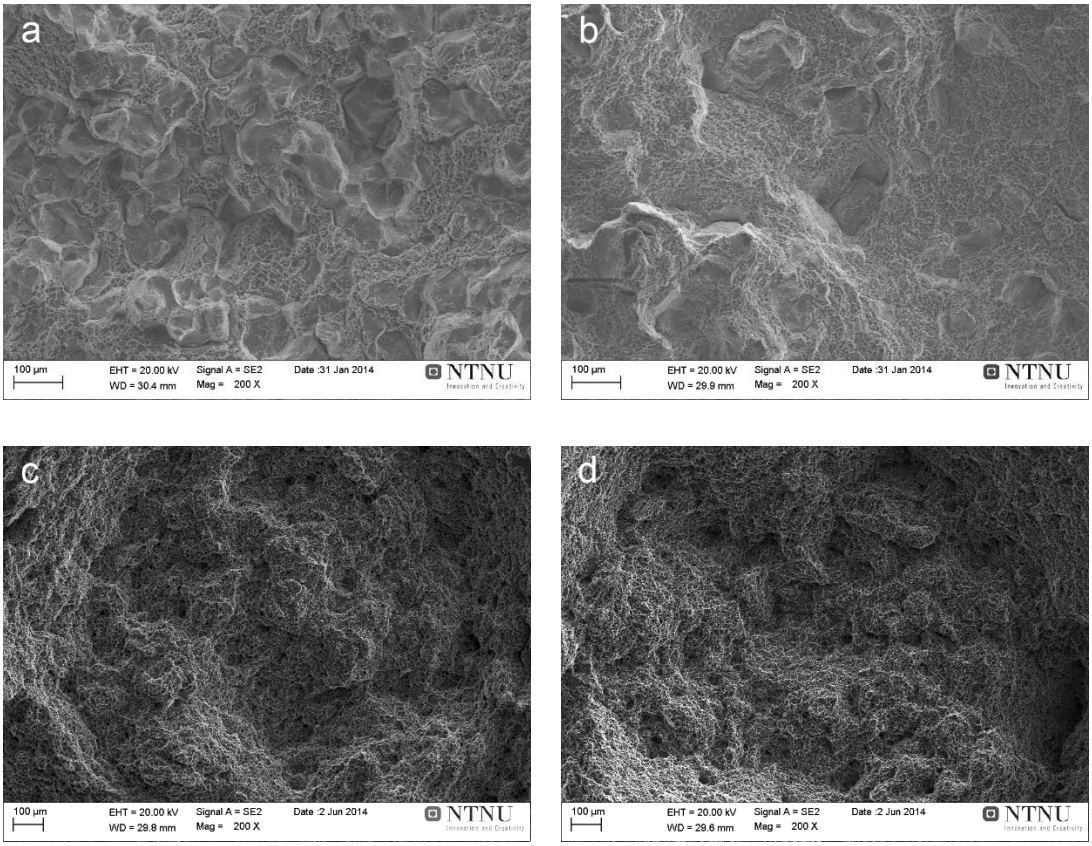

Figure 4.12: SEM images of the fracture surfaces at 200X, showing variations in dimple fractions of 6181 (a), KFC (b), 6082 (c) and KK13 (d).

The 6181 alloy showed clear signs of intergranular fracture, as seen in Figure 4.13a, with dimple formations also present between the faceted "rock candy" formations. KFC displayed the same behavior, but in addition to this, a surface texture similar to "river lines" was present on some grain surfaces. These are often found as a result of fracture by cleavage (section 2.3.2.2).

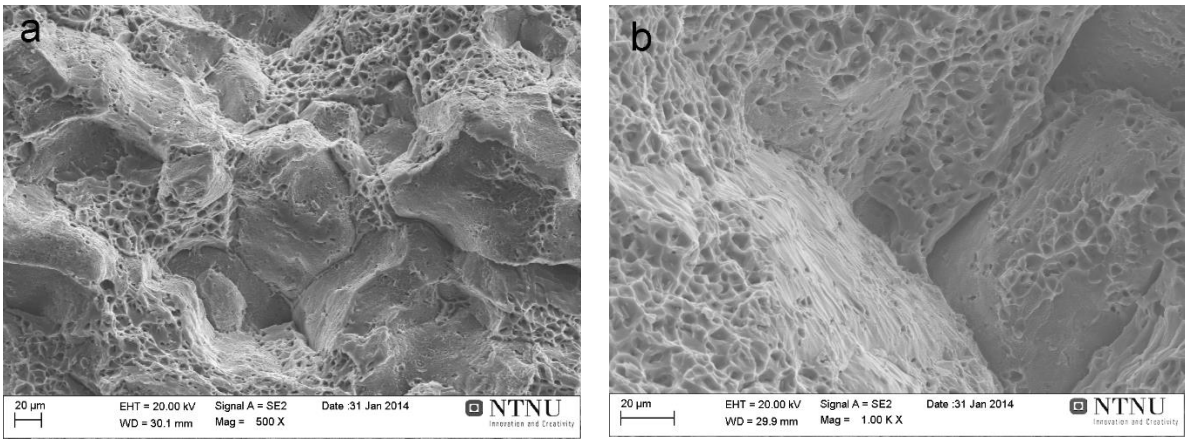

Figure 4.13: SEM images of intergranular fracture. a) Intergranular fracture mode with dimples between the facets in 6181 at 500X. b) Intergranular fracture and a formation similar to cleavage mode, with parallel lines along the fracture surface in KFC at 1000X.

Figure 4.14 displays the presence of primary particles inside some of the dimples, and shows their highly elongated shapes. This was quite easy to observe in the case of 6181 and KFC, due to their more shallow dimples. In the case of 6082 and KK13 it proved to be more difficult, as they were often hidden in the deeper dimples.

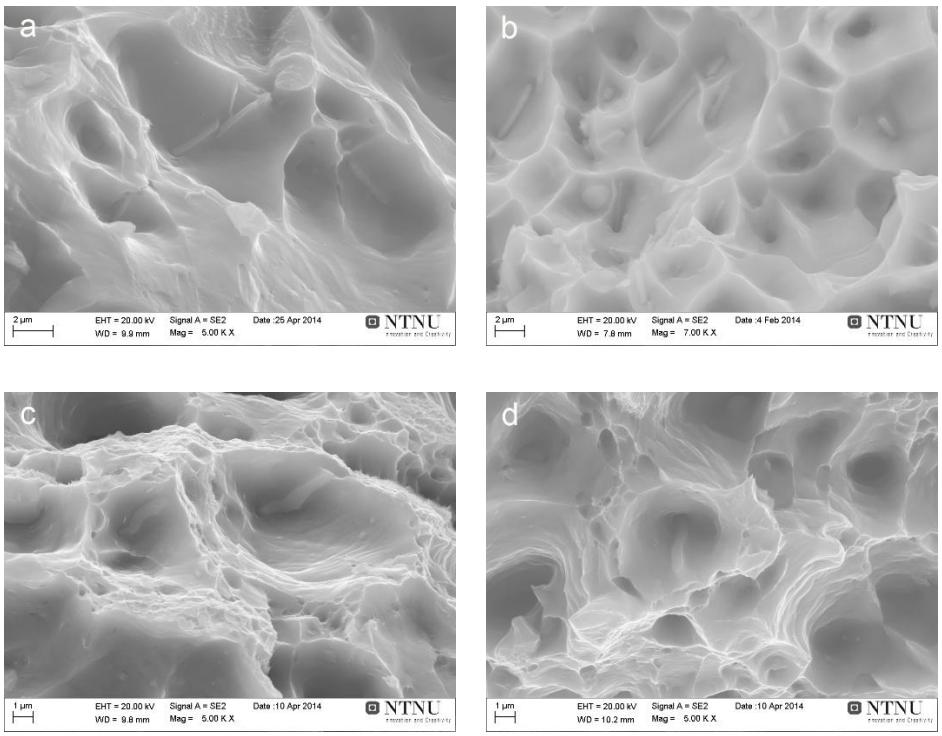

Figure 4.14: SEM images showing the presence of particles inside the dimples. Note: 6181 (a), 6082 (c) and KK13 (d) were taken at 5 kX, and KFC (b) at 7 kX.

Concentrating on the facets of 6181 and KFC, shallow dimples with visible particles were evident. This is shown for 6181 in Figure 4.15a, while the corner of a facet in KFC is shown at higher magnification in Figure 4.14b.

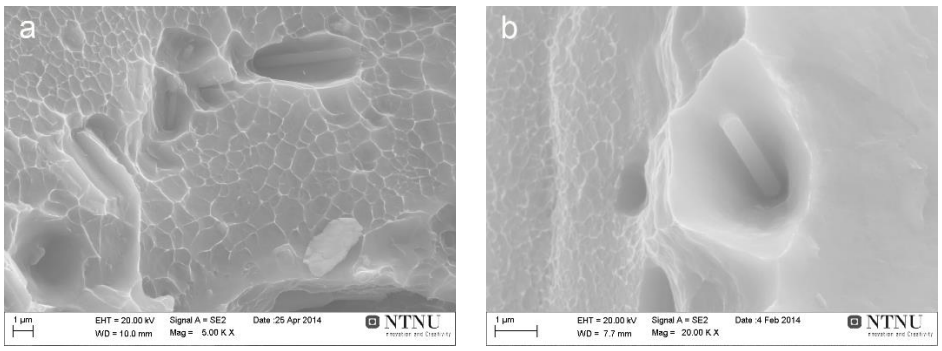

Figure 4.15: Dimples on facets. a) Particles present in shallow dimples on the surface of a facet in 6181 at 5kX. b) is an image from the corner of a facet in KFC at 20kX.

In 6082 and KK13 one could search for a dimple with the right angle, and see inside the "cave" of the dimple to observe the presence of particles. Figure 4.16 shows such an example for 6082 and KK13, for which the use of this technique was often necessary, to observe the particles inside.

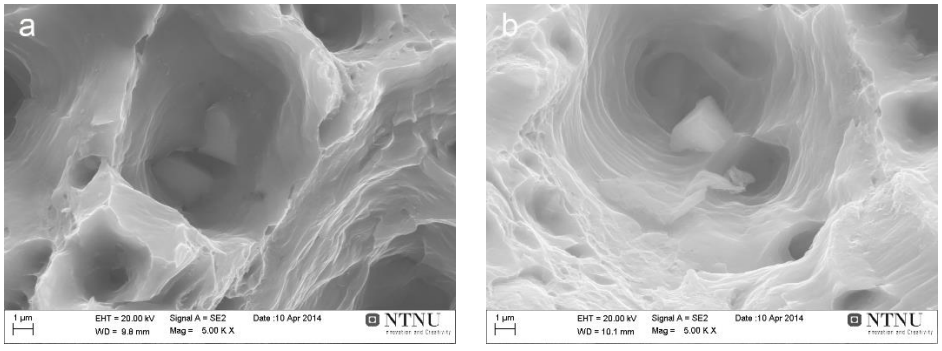

Figure 4.16: Deep dimples. SEM images of 6082 (a) and KK13 (b) at 5kX showing particles inside deep dimples.

4.6 Transmission electron microscopy

TEM imaging was performed to obtain information unavailable through other methods. In terms of strength and ductility, the geometry, distribution, and number density of the precipitates are important, and it was therefore of high interest to get clear observations of the

differences in these factors. In addition, it was desirable to examine the possible presence of grain boundary precipitates and of a sub-grain structure, along with dispersoid characteristics, and the presence and width of the PFZ. Quantitative measurements were not executed, as the main target of this investigation was to obtain a qualitative impression of the respective characteristics. Additional images may be found in Appendix C.

4.6.1 Precipitate distribution, shapes and sizes

The precipitate distribution is displayed in Figure 4.17, and shows clear contrasts in terms of precipitate geometry and density. The width or thickness of the precipitates seemed to be larger in 6181 and 6082 compared to the two Cu-containing alloys. Both KFC and KK13 had a thinner shape, while in KFC the precipitates were more elongated than for the KK13 alloy. The latter also had a denser particle distribution compared to the other alloys. It may seem as if 6082 had the lowest precipitate density, while 6181 and KFC were hard to tell apart.

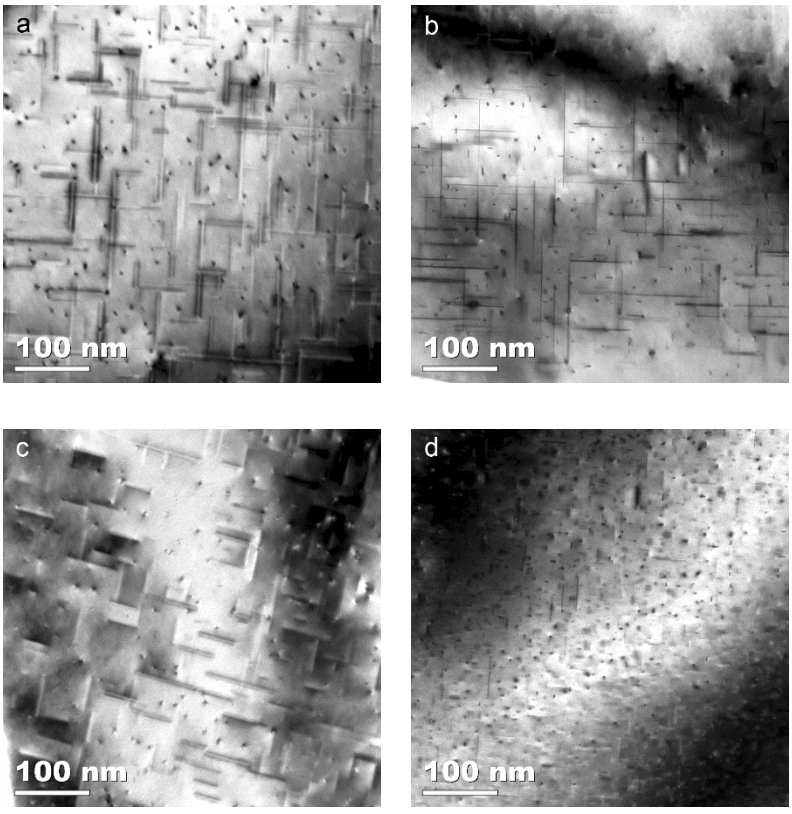

Figure 4.17: The precipitate distributionof 6181 (a), KFC (b), 6082 (c) and KK13 (d), shown at 40kX.

Figure 4.18 demonstrates more clearly the differences in precipitate size and shape. From these images it seems safe to assume that the precipitates of the non-Cu alloys are thicker compared

to KFC and KK13. The two latter are hard to tell apart in terms of thickness, but it seems as if the precipitates in KK13 are both somewhat thinner and shorter in length.

Another interesting observation from the 100kX images is the shape of the precipitates orientated along the beam axis, represented as dark spots. For both 6181 and 6082, these have a more or less circle-shaped cross-section. This type of cross-section is also found in the two Cu-containing alloys, though in a lesser amount. For these, there is clear a indication of the presence of a different shape, more precisely a rectangular cross-section, corresponding to lath-shaped precipitates [26].

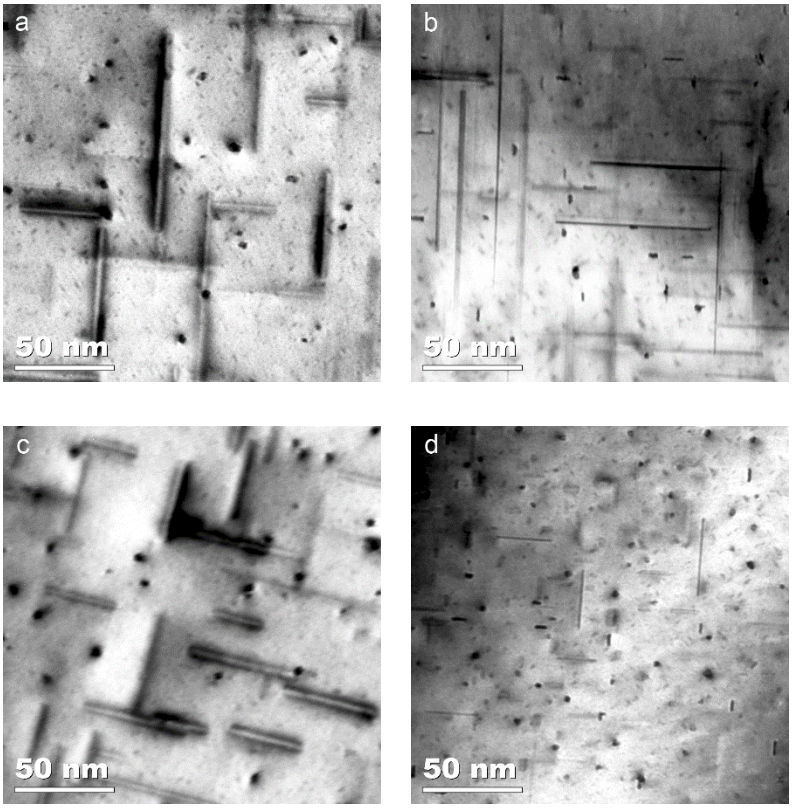

Figure 4.18: Precipitate distribution and sizesof 6181 (a), KFC (b), 6082 (c) and KK13 (d), imaged at 100kX.

4.6.2 Grain boundary precipitates

Grain boundary precipitates were found in KFC, 6082 and KK13. It was not successful to observe these in 6181, though it does not exclude their presence.

The grain boundary precipitates found in KFC, and displayed in Figure 4.19, appeared coarser than for 6082 and KK13, but for all alloys they were numerous and easily observed. In KK13,

they seemed to have a certain directional preference, oriented in more or less the same direction as the precipitates in the grain on the left hand side in Figure 4.19c. The grain boundary also seemed to be affected by this, obtaining a jagged shape.

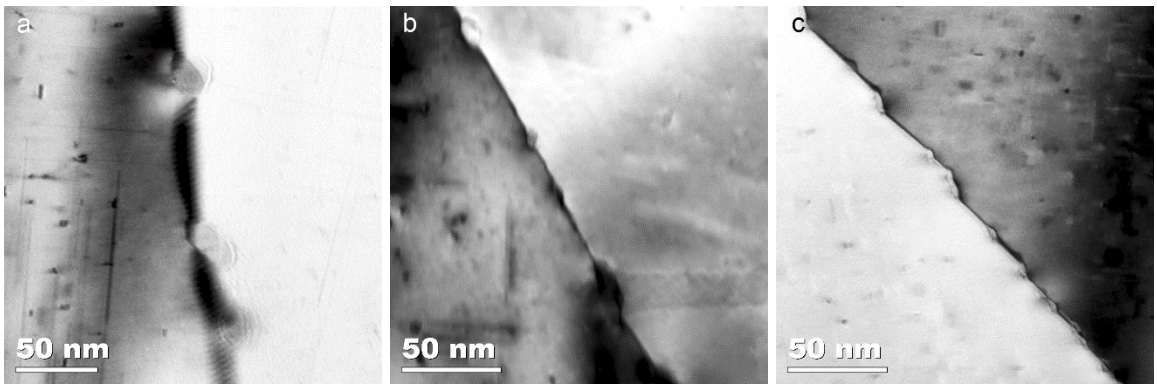

Figure 4.19: Grain boundary precipitates of KFC (a), 6082 (b) and KK13 (c), visualized at 100kX.

4.6.3 Precipitation free zone (PFZ)

The characteristics of the PFZs are shown in Figure 4.20. A rough measurement of the widths of the PFZs in 6181 and 6082 resulted in 29.5 and 38 nm, respectively, while the PFZ in KK13 was the narrowest, with 21 nm. In the case of KFC it was not successful to obtain a clear view of the PFZ by any grain boundaries investigated, and is likely to be due to an unsuitable tilting angle.

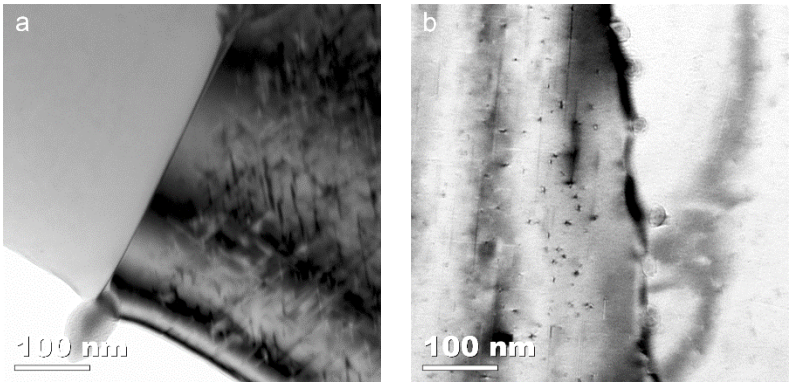

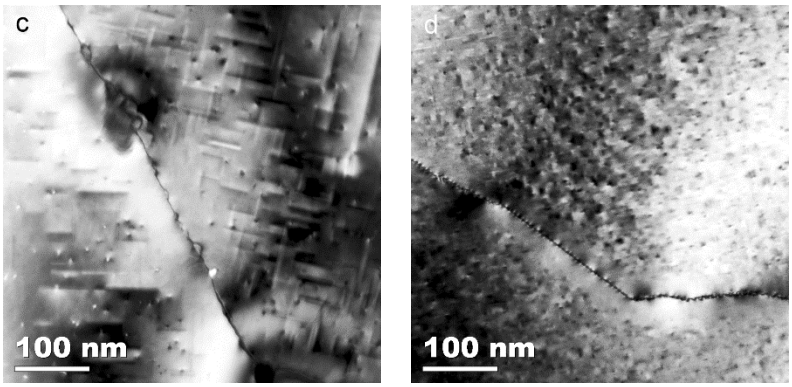

Figure 4.20: TEM images of the precipitation free zone (PFZ) in 6181 (a), KFC (b), 6082 (c) and KK13, visualized at 40kX.

4.6.4 Dispersoids

In general, the dispersoids observed in 6082 and KK13 were smaller and more numerous compared to the alloys without additions of Mn. These relatively small dispersoids were found on the grain boundaries, and in grain boundary junctions, as well as submerged in the matrix. Figure 4.21 demonstrates a high density of dispersoids, and their pinning of the grain boundaries in the Mn-containing alloys.

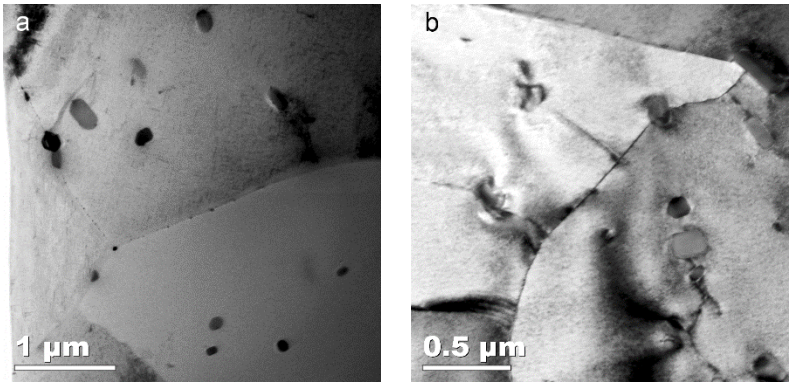

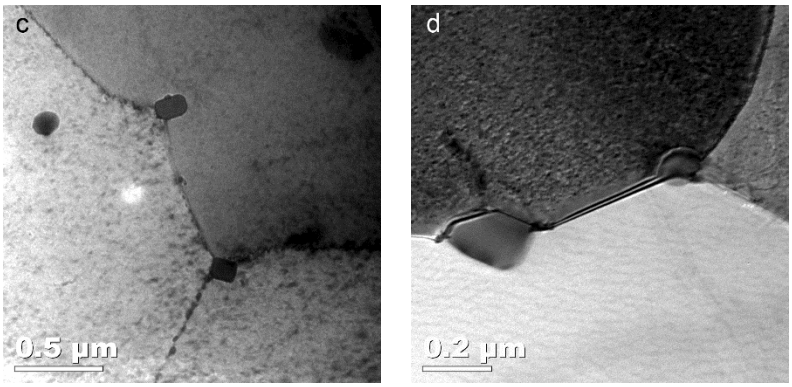

Figure 4.21: TEM images of dispersoids in 6082 at 5kX (a) and 20kX (c), and KK13 at 10kX (b) and 20kX (d).

In the case of 6181 and KFC the amount of small particles or dispersoids observed were fewer in number, and generally coarser in character. Some of these larger dispersoids were found on grain boundaries and are displayed in Figure 4.22.

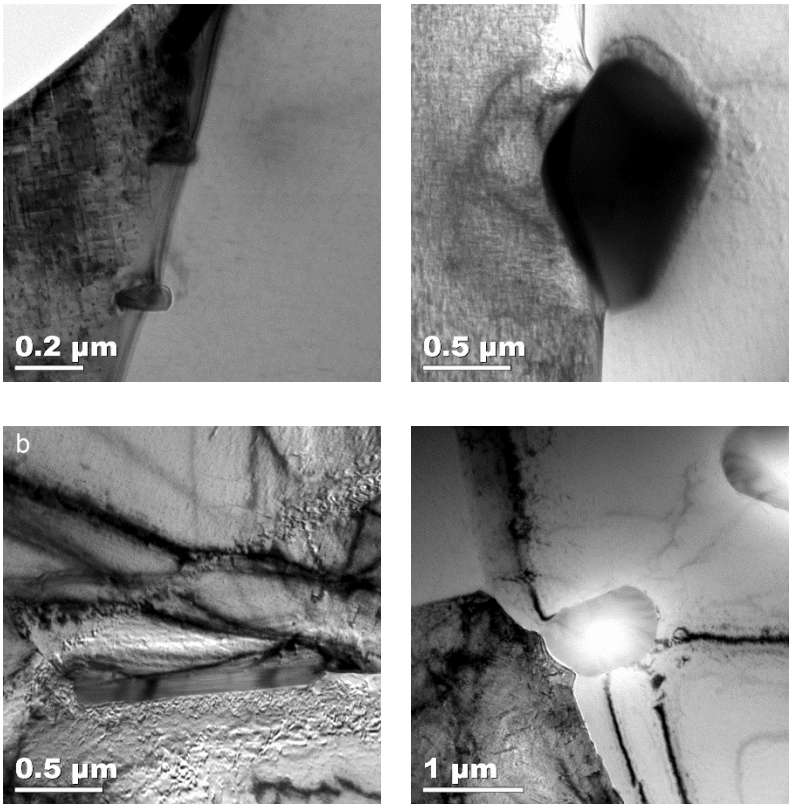

Figure 4.22: TEM images of dispersoids and grain boundary pinning. a) Small dispersoids on a grain boundary in 6181 (20 kX). b) A coarse dispersoid in 6181 (10 kX). c) and d) Dispersoids in KK13 (10 kX and 5 kX, respectively).

4.6.5 Sub-grain structure

A sub-grain structure was not found in all the alloys, and it was, as expected, only observed for the two Mn-containing alloys, 6082 and KK13. These generally displayed a small grain size, and a high density of low-angle grain boundaries. Low-angle grain boundaries are illustrated in Figure 4.23c and d, where the diffraction patterns taken at the grain boundary between the two top grains clearly indicate a small orientation difference. KFC also displayed a similar behavior, with a larger amount of grains observed, including low-angle grain boundaries, as compared to the 6181 alloy. However, it was not successful to obtain a clear diffraction pattern at these grain boundaries. Even so, Figure 4.23a shows the relatively small orientation difference between two grains in KFC.

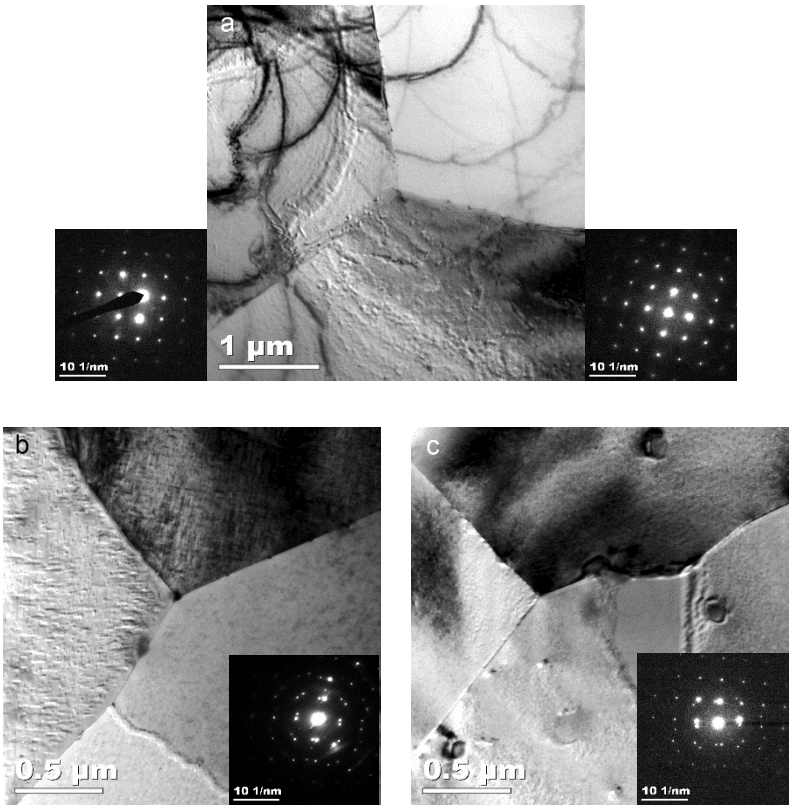

Figure 4.23: Images with diffraction patterns revealing the presence of sub-grains in 6082 (b) and KK13 (c), and a low-angle grain boundary in KFC (a). a) A low-angle grain boundary for which the diffraction patterns are taken from the top right and left grains respectively. In b) and c) the diffraction images are taken from the grain boundaries.

5 Discussion

5.1 Ageing behavior and electrical conductivity

The ageing curves in Figure 4.1 may be divided in two stages, in relation to what occurred between 0 min and 1 hour, and the development after 1 hour had passed. A rapid increase in hardness for the Cu-containing alloys was observed in the initial stages, and is expected to be due to the formation of a different type and density of atomic clusters and GP-zones [27]. As mentioned in section 2.2.3.3, Cu has been observed to form needle-shaped and fully coherent GP-zones in the initial stages of ageing, which may contribute in explaining this behavior.

Excess-Si is also expected to have a catalytic effect on the nucleation of GP-zones, but no hardening effect from the two excess-Si alloys without Cu (6181 and 6082) was seen until 1 hour had passed. The fact that the Mg-rich KK13 alloy increased in hardness at a much higher rate than 6181 and 6082 indicates that Cu has a much larger importance in this early stage than excess-Si. However, the relation is reversed after 1 hour, when the KK13 graph flattens, and increases very slowly in hardness until peak hardness is reached. In this stage, the excess-Si alloys display their largest hardening rate, including the Cu-containing excess-Si alloy KFC. The Mn-containing excess-Si alloy 6082 has a somewhat lower increase than 6181 and KFC after 1 hour, which could be due to a depletion of Si in the formation of dispersoids. Based on these observations, a hardening effect due to an addition of excess-Si therefore only seems to be associated with the later stages of ageing, although the basis may have originated from earlier ageing times, through the formation of a finer dispersion of atomic clusters and GP-zones [23, 25].

The electrical conductivity of the alloys, in Figure 4.2, shows a certain correspondence to the ageing curves. The excess-Si alloys 6181, 6082, and KFC display a sharp increase in conductivity after approximately 1 hour, which coincides with the hardness increase in the ageing curves. The order in which the curves of these alloys are positioned in relation to one another in terms of electrical conductivity also corresponds well with their alloying content. 6181 consistently displays the largest conductivity, and is also the least alloyed of the materials involved. KFC contains the same amount of Mg and Si as 6181, but the addition of Fe and Cu has resulted in a lower conductivity. However, according to Equation 5, Cu does not have a large effect on this property, and although Fe does, more or less all of the Fe is expected to be removed from solid solution in the formation of constituents. Although the constituents are not likely to be coherent, they may still create deformation fields [5], leading to a larger reduction

in electron mobility in KFC, although it is uncertain to which degree this applies. Perhaps a more likely explanation is the possible presence of a different precipitation structure or coherency of the atomic clusters and GP-zones, as KK13 also has a very low conductivity in the initial stages.

The 6082 alloy has an addition of 0.55 wt% Mn, and its graph is consequently positioned below 6181. Even if most of the Mn is bound in dispersoids and constituents, a certain amount will remain in solid solution. The afore-mentioned deformation field caused by particles may contribute in explaining its lower conductivity as compared to 6181.

5.2 Constituents

5.2.1 Chemical composition

In addition to the uncertainty related to the actual volume analyzed in the EDS analysis, which was discussed in section 4.3.2, one should keep in mind that a selection of 6-8 particles of an alloy does not provide a statistically reliable representation of the alloy as a whole. Nonetheless, it does provide an indication of what may be present, as the constituents were chosen at random.

At least half of the constituents in both 6181 and KFC seemed to be of the β-AlFeSi type, which, as discussed in section 2.2.2.1, is known to be of negative consequence to the formability and ductility of 6xxx alloys. Results suggesting the presence of the usually less detrimental α-$Al_{12}Fe_3Si$ could perhaps account for the other half of the constituents, but the signals obtained were somewhat diffuse and it is difficult to affirm with any certainty. In a study performed by Kato et.al, an increase in ductility was found for an increasing Fe-content in 6xxx alloys with excess-Si [22]. It could be suggested that by increasing the Fe content, a larger amount of smaller α constituents could be formed during casting, on the expense of coarse β-constituents, due to a difference in diffusivity of Fe and Si, but no such relation was found from the results in Figure 4.9. The KFC alloy did display a larger ductility than 6181, but this is expected to be due to changes in the ageing behavior with the addition of Cu. Additionally, in a recent study executed to confirm the findings of Kato et.al, no positive effect was found increasing the Fe-content [49].

The compositions of the constituents found in 6082 and KK13 were somewhat ambiguous, and did not give a sufficient match to constituents suggested by the literature to be found in these alloys (section 2.2.2.1). With the strong signal from Fe, one could expect a correspondence to α-$Al_{15}(FeMn)_3Si$ or $Al_8(FeMn)_2Si$, but the weak signal from Mn suggests the presence of

another phase. Regardless of their uncertainty, the results at least give a rough idea of the amount of alloying element which have been removed due to the formation of constituents.

An interesting observation from the results of KK13 is the higher concentration of Cu indicated in Figure 4.9. Cu is unlikely to take part in the constituent composition, but it can be speculated that the signal results from a different precipitation behavior around the particles, as a result of the increased dislocation density in these areas compared to the matrix. It could also be speculated that it comes as a result of incomplete dissolution of the $Al_{1.9}CuMg_{4.1}Si_{3.3}$ phase during homogenization [13, 14], and diffusion effects related to this (section 2.2.2.1).

5.2.2 Distribution and size

Due to the low solubility of Fe in the aluminum matrix [10], the distribution and sizes of the constituents were expected to be more or less in correspondence with the Fe content. This was also evident for KFC which contained both a higher number density and coarser particles, while covering a larger area than the alloys with ~0.20 wt% Fe (Table 4.6). 6181 may be compared directly to KFC, as Cu is not expected to contribute to the constituent formation. Relating the ratio of wt% Fe_{KFC} and Fe_{6181} (=2.27) and the ratio of the number of particles in the respective alloys (=2.29) one obtains a clear correspondence. The ratio of the respective area fractions yields a similar result (=2.63), and further establishes this relation. Without comparing more alloys with different Fe content, one should perhaps be careful to draw the conclusion of such a strong relation, but it is nonetheless an interesting observation. The particle sizes however, are more or less equal for both 6181 and KFC, indicating an independence of Fe content on this characteristic.

6082 and KK13 contained both larger and a higher number of constituents than 6181. This can be assumed to be due to the presence of Mn, giving a larger amount of available atoms for constituent formation. Between these two, a slightly larger number of particles was observed in KK13, while the average size was larger for 6082. As constituents are known to grow partially by diffusion from a super-saturated matrix during homogenization (section 2.2.2.1), it seems reasonable to propose that the lower Si content in KK13 may result in smaller particles. It could therefore be suggested that the nucleation or formation of particles is similar during solidification, resulting in a similar number of particles, while the larger amount of available Si in 6082 leads to extended growth. The latter may also explain the findings in Figure 4.8, where particles with an ECD larger than 4.5-6 µm were observed for all alloys except KK13.

The way the distribution in Figure 4.8 is shifted slightly towards smaller particles for 6082 and KK13, as compared to 6181 and KFC, indicates that a slower diffusion of Mn relative to Si results in a slower growth rate of the constituents, leading to smaller particles.

5.3 Grain structure

The inhomogeneous grain sizes found in the recrystallized alloys in Figure 4.10 would be expected to result in a more inhomogeneous deformation behavior, leading to a reduction in ductility. The differences in grain sizes could be due to the non-uniform spatial distribution of constituents, as indicated by Figure 4.7, assuming the main recrystallization mechanism is PSN. However, with the latter being the case, smaller grain sizes would be expected in KFC as compared to 6181. EBSD scans indicated similar grain sizes, with the average grain size of 6181 being slightly lower, which suggests that another recrystallization mechanism also operates, perhaps by nucleation from transition bands, or due to impurities leading to a difference in the formation of dispersoids in the two alloys, which may hinder nucleation and slow down recrystallization kinetics. Dispersoids were found in investigation by TEM (Figure 4.22), and some of these did seem to have had a pinning effect on the grain boundaries.

The grain structure was clearly fibrous in 6082 and KK13, i.e. not recrystallized, resulting from the addition of Mn, forming dispersoids. TEM images (Figure 4.21) revealed a large amount of small dispersoids pinning grain boundaries and grain junctions. The presence of these dispersoids has obviously given a strong resistance against recrystallization, and resulted in the subgrain-structure illustrated in Figure 4.23, with much smaller average sizes (section 4.4).

5.4 Fractography

5.4.1 Decrease in cross-sectional area after fracture

The difference in cross-sectional area measured before and after fracture, with laser extensometer and SEM, respectively, showed a larger difference for 6082 and KK13 than for 6181 and KFC. This could suggest a coherence with the grain morphology, as the former contained vastly elongated grains. However, as 6181 and KFC displayed a far lower ductility than 6082 and KK13, it is also possible that it comes as an effect of ductility, or total elongation.

Literature does not provide any studies on the reduction in cross-sectional area observed after fracture, perhaps due to the lesser use or unavailability of laser extensometers in earlier years. The elastic region of the stress-strain curve could explain a very small *increase* in cross-sectional area, but what is observed is a relatively large *decrease*. A possible theory to explain

the behavior arises from the Bridgman analysis [34], which suggests the presence of tri-axial stresses in the specimen in tension. It could be imagined that a driving force for contraction is inherent in the neck during tension, as voids increase in number and size, but that the material is held back from contracting due to the presence of the larger axial stresses in the tension direction. As the tensile specimen finally fractures, the axial forces let up, and the necking region is forced inwards.

5.4.2 Fracture surfaces

The fracture surface images provided in Figure 4.12 revealed a combined effect of intergranular and ductile fracture mode as the cause for fracture in 6181 and KFC. The dimple fraction however, was notably smaller for 6181, which made the failure to observe grain boundary precipitates in this alloy somewhat surprising. The relatively low ductility was expected from what is known about excess-Si alloys in the literature [25], and one would expect to relate this to the precipitation of coarse particles at grain boundaries. Whether it comes as an effect of grain boundary precipitates, or a different deformation behavior of the PFZ remains unknown, but the larger fraction of intergranular fracture surfaces is assumed to be due to one of the afore-mentioned theories.

Although more common in brittle materials, KFC showed suggestion of cleavage mode in addition to ductile and intergranular fracture modes. The image in Figure 4.13 displays a texture of the fracture surface similar to what is known as “river lines”. There are visible parallel lines along the surface, which could originate from slip on parallel planes if the critical cleavage stress had been reached [43]. This was seen for many facet surfaces in KFC, while absent in 6181. The evidence is not sufficient to conclude that cleavage is the source of these lines, but in the very least it indicates a different fracture/deformation behavior of KFC with respects to 6181.

The completely ductile behavior of 6082 and KK13 clearly suggests that a more homogeneous deformation has been caused by the presence of a sub-structure due to the addition of Mn. Additionally, the smaller grain boundary precipitates found in these alloys reduces the risk of intergranular fracture.

Figure 4.14-16 display visible particles which were found inside the dimples of all alloys. The deeper dimples in the two Mn-containing alloys is likely to be due to the larger ductility, resulting in an extended elongation of the dimple/void walls. In 6181 and KFC, the small and

shallow dimples found on the fracture surfaces, suggests a void formation has taken place prior to intergranular fracture.

5.5 Transmission Electron Microscope

5.5.1 Precipitate distribution

If one assumes the precipitates of the same type, size and shape are involved, a larger precipitate density would result in a larger degree of hindering dislocation movement, and thus increase in strength. The images in Figure 4.17 indicate a clear difference in precipitate number density, although it may not be a completely reliable impression due to the thickness factor. A larger sample thickness would result in a larger amount of visible precipitates as a larger volume is involved, leading to a false impression. The sample thickness was not measured for these specimens, and the precipitate density must therefore be evaluated with caution.

From Figure 4.17 it seems that 6082 contains the lowest density of precipitates, while KK13 the highest. As Mn and Fe does not contribute to precipitate formation, their differences must be an effect of wt% Si, wt% Mg, and wt% Cu. Excess Si is expected to contribute to a finer distribution of precipitates [23, 25], but it seems evident that Cu has had a larger effect, when comparing these two alloys. However, this is not clear from KFC, containing both excess-Si and Cu. Although the image quality is not optimal, there does not seem to be a large difference in precipitate number density as compared to 6181- The differences seem to be mainly with respects to the size and shape of the precipitates. This suggests the addition of excess-Si in the Cu-containing alloys does not have a large effect on the spatial precipitate distribution, while on the contrary, the large amount of Mg in KK13 seems to have had a positive effect. A possible reason may be that the precursory phases to Q' ($Al_3Cu_2Mg_9Si_7$) have a similar stoichiometry, and that they consequently require higher levels of Mg for their formation, as compared to β'' (Mg_5Si_6) [27].

The lower precipitate density suggested for 6082, compared to 6181, seems surprising due to the similar amount of hardening alloying elements in both alloys. This may however be explained by the involvement of Si in the formation of dispersoids and constituents, leaving less Si available for precipitation after casting and homogenization in 6082. On the other hand, this would also result in a further depletion of Si in KK13, although Table 4.6 indicated a somewhat lower volume fraction of constituents are present here.

5.5.2 Precipitate sizes and shapes

The size and shape factors are also important for the resulting strength, as smaller coherent precipitates at high densities usually give the most desirable mechanical properties. In Figure 4.18, it is clear that the presence of Cu has resulted in different precipitate sizes and shapes. KFC and KK13 both seem to contain much thinner precipitates than 6181 and 6082, while KFC had a larger extension in the <100>-direction of the two Cu-containing alloys. The distinct needle shaped precipitates observed in KFC were not observed in the other alloys, but may also have been overlooked in KK13 as small needles are somewhat more difficult to spot. The larger extension of the precipitates in KFC as compared to KK13, and in 6181 as compared to 6082, may be due to the larger amount of Cu and/or Si available for their growth. A rectangular cross-section in some of the precipitates in KFC and KK13, could possibly belong to the L phase, contributing to additional hardening in these alloys [26, 27].

Needle shaped particles were expected in all alloys, in the form of either β'' or precursory phases to Q'. The reason for their absence is unknown, but could be due to various factors, such as over-ageing or different precipitate types at peak strength.

5.5.3 Grain boundaries

Due to the obvious intergranular fracture facets frequently observed on the 6181 fracture surface, it was a surprise that no grain boundary precipitates were found in this alloy. Figure 4.20 clearly shows a PFZ in 6181, with more or less the same width as in the other alloys. From what was presented in section 2.2.3.5, two mechanism may explain the formation of PFZs. The PFZ in 6181 may have mainly resulted from the formation of grain boundary precipitates, but they were not found to any significant degree. It may therefore be suggested that the absence of sufficient vacancies after solid solution heat treatment has given the larger contribution to the formation of the PFZ for 6181, leading to a supersaturated PFZ instead of one depleted of alloying elements. However, this alternative seems unlikely to be the cause of intergranular fracture as the reason for the latter has often been related to the relative ease by which one may deform a depleted PFZ [33]. A super-saturated matrix would result in more resistance to deformation, and a larger degree of work-hardening as compared to one that is depleted. The intergranular fracture mode associated with this alloy is therefore assumed to have come as an effect of fewer, but coarser grain boundary precipitates, or perhaps coarse dispersoids/particles on the grain boundaries.

In KFC, relatively large grain boundary precipitates were found, and could be due to the larger amount of excess-Si available for diffusion to grain boundaries. No satisfactory image of the PFZ was obtained, but this is likely to be due to coincidences, rather than its complete absence. In comparison, the KK13 alloy contained far smaller grain boundary precipitates, which were also partially oriented with the neighboring grain. The small amount of Si available seemed to be favorable for the avoidance of coarse grain boundary precipitates.

The precipitates found at the grain boundaries in 6082 were less coarse than in KFC, which is likely to be due to the participation of Si in dispersoid formation.

5.5.4 Dispersoids

Figure 4.22 revealed small particles or dispersoids on the grain boundaries in 6181 and KFC, some of which were of such a nature that it gives rise to a speculation of the possible presence of impurities, such as transitions metals like Cr or Mn. If present, they are in such a small concentration that they have not affected recrystallization to any large degree, but they could have had an effect on the grain growth. An inhomogeneous distribution of dispersoids and particles could contribute to explaining the inhomogeneous grain sizes for the recrystallized alloys. The intentional addition of Mn in 6082 and KK13 has led to the formation of numerous smaller dispersoids, which have effectively resisted grain boundary movement (Figure 4.21), resulting in a fibrous structure with small (sub-)grains.

5.6 Tensile tests

5.6.1 Aged specimens

When comparing the ageing curves (Figure 4.1) with the stress-strain curves (Figure 4.3), a superior performance in terms of strength/hardness is revealed from the Mn-containing alloys in tension, relative to the hardness tests. Their elongated grain morphology, is suspected to be one of the reasons for this, as the hardness tests were taken in the RD-RD plane. If taken in the RD-ED plane, one could perhaps expect their peak hardness values to correlate better with the strength displayed in the stress-strain curves, relative to 6181 and KFC. These alloys also displayed the best ductility, which is likely to be attributed to their inherent sub-grain structure resulting in a more homogeneous deformation distribution. The fact that these alloys also had smaller constituent sizes and smaller grain boundary precipitates aids in explaining this behavior.

As an excess-Si alloy, 6082 displayed a far better property balance than 6181, which is quite evidently due to the addition of Mn. The combination of a subgrain structure, smaller and less harmful particles/dispersoids at grain boundaries, and the lower availability of free Si for the detoriation grain boundaries is the expected reason for their deviant performance.

It is also apparent that the addition of Cu has improved the balance of mechanical properties in the respective alloys. The cause for this however, is somewhat less evident. KFC did not display decisively preferable characteristics in the microscopic analysis to explain its superior ductility with respect to 6181. The assumption is that the different precipitate size, shape and structure revealed by TEM imaging, along with the observed differences in grain boundary characteristics are the decisive factors.

With the above-mentioned, one would not be too surprised to see KK13 displaying by far the best properties of all the alloys involved, in terms of both strength and ductility. This result emphasizes the positive effects of a combined addition of Mn and Cu on the mechanical properties, although it partially contradicts earlier findings on the significance of excess-Si in Al-Mg-Si alloys [23, 25]. In any case, the balanced alloy had the best balance of properties in this study.

Even if precipitates in Cu-containing alloys at peak strength contained a larger amount of Mg than what is common in conventional Al-Mg-Si alloys, the KK13 alloy seems to contain Mg in excess relative to the expected hardening phases. It could therefore be suggested that some Mg remains in solid solution, resulting in a strength contribution. The rapid work hardening at lower strains suggest this, but the relation may not be confirmed by the investigations performed in this thesis.

5.6.2 The effect of pre-straining from T5

The tensile specimens which had not received additional heat treatment after extrusion were labeled with temper T5. The results of the tensile tests from the pre-strained T5 specimens showed an interesting behavior in 6082. They had only been subjected to natural ageing, and displayed a larger work hardening than the T6 specimens, resulting in a superior strength without the loss of ductility. The presence of alloying elements in solid solution is expected to generate more dislocations than in the T6 alloy, resulting in the different work hardening observed in the initial stages. Even though these alloys have been naturally aged for approximately one year after extrusion, the effect of natural ageing is expected to saturate after

a few weeks [50]. Pre-straining could therefore be an interesting prospective in the production of 6082 alloys, as an alternative to artificial ageing, without a loss of strength and ductility.

The same behavior was not observed for KK13, where both the pre-strained T5 specimen, and its aged parallel, displayed a lower toughness than for T6. A possible explanation could be the differences in diffusion rates of the elements in the respective alloys, resulting in different type of atomic clusters and GP-zones during natural ageing. This is partially indicated by the hardening and electrical conductivity curves, where the precipitation characteristics are highly different in the two alloys.

The specimens that were aged after pre-straining in T5 all seemed to have over-aged both for 6082 and KK13. As the natural ageing was 1 year, as compared to 4 hours for the T6 alloys, this is not surprising as they were given the same artificial ageing treatment. It could therefore be interesting to see the possible effects of lowering the artificial ageing times and/or temperature, to find peak hardness. The dislocations generated by pre-straining could give a finer precipitate distribution due to the preferred nucleation of precipitates on dislocation, which could improve the mechanical properties.

5.7 Suggestions for future work

The results of this thesis has given a basis for considering several additional experiments or studies. The most interesting prospects are considered to be the following:

- It is not certain if the balanced Mg/Si ratio in KK13 is beneficial for the strength and ductility of the alloy. The results indicate such a correspondence, but as the Cu-containing alloy with excess-Si, KFC, does not contain Mn it is uncertain if the superior strength of KK13 is contributed by the balanced Mg/Si ratio. Varying the content of Si, and holding the other alloying content constant, should yield a better understanding of this relationship.
- The effect of Cu on the ductility of Al-Mg-Si alloys is not revealed from this thesis. The strengthening effect of Cu is well established, but the mechanisms for an increase are not quite clear. To observe its effect, similar experiments could be conducted on alloys with a varying Cu-content, looking at variations in precipitation, grain boundary, constituent characteristics etc.
- The pre-strained tensile test samples which had been artificially aged all seemed to have over-aged. Ageing curves should be produced after pre-straining to find the holding

time to peak hardness, so that new tensile tests may be performed to give an improved answer to the effect of ageing.

- Pre-straining could also be performed on T5 samples which only ages naturally for a few weeks. This ageing time would give a better answer to the practical benefit of pre-straining.

6 Conclusion

Experiments were conducted to attempt to understand the effects of different alloying content on the ductility of Al-Mg-Si alloys. Mechanical testing along with examinations of grain, constituent, precipitatation and fracture characteristics was performed on four alloys with different concentrations of Si, Mg, Fe, Mn and Cu. On the basis of these results the following conclusions may be drawn:

- The Cu-containing alloys increased rapidly in hardness during the first hour of ageing. After this point, the excess-Si alloys displayed the most rapid increae in hardness.
- A clear correspondence between Fe-content and constituent number density and area fraction was found. However, no difference in average constituent size was observed with dissimilar Fe-content.
- The presence of excess-Si, without additional alloying elements, resulted in a significant reduction in ductility, leading to the observation of intergranular fracture. The introduction of Fe and Cu improved this behavior, possibly due to the formation of secondary phases with Fe and Si, leaving less free Si available for detoriation of grain boundaries.
- Mn had the largest positive effect on ductility, which was related to a resistance to recrystallization and grain growth, induced by Mn-containing dispersoids, resulting in a fine subgrain structure. The introduction of Mn also reduced the average constituent sizes by formation of different constituents and dispersoids. The latter is assumed to have resulted in smaller and less damaging micro-voids.
- The introduction of Cu gave a significant increase in strength, without a serious reduction in ductility. This confirms previous studies, and is likely to be due to a change in precipitation behavior. Lath shaped precipitates were observed, which could correspond to the hardening L-phase previously observed in Al-Mg-Si-Cu alloys. A finer precipitation size and distribution was also observed for these alloys.
- Adding Mn and Cu to a balanced alloy gave the best combined properties in terms of strength and ductility. The combination of a fine subgrain structure, precipitation size and distribution, and smaller secondary phases is considered to be the likely cause.

7 References

1. Ø. Breivik, K.W. *Mener aluminium er framtidens offshore-metall*. 2013 03.12.13; Available from: http://www.hydro.com/no/Hydro-i-Norge/Pressesenter/Nyheter/2013/Mener-aluminium-er-framtidens-offshore-metall/.
2. Polmear, I.J., *Light Alloys: From Traditional Alloys to Nanocrystals*. 4 ed. 2006: Elsevier.
3. Solberg, J.K., *Teknologiske metaller og legeringer*, NTNU, Editor. 2010.
4. Graeve, I. and J. Hirsch. *6xxx Series Alloys*. 04.06.14; Available from: http://aluminium.matter.org.uk/content/html/eng/default.asp?catid=214&pageid=2144417085.
5. Verlinden, B., *Thermo-Mechanical Processing of Metallic Materials*. Pergamon Materials Series, ed. R.W. Cahn. 2007: Pergamon.
6. Reiso, O., *Extrusion of AlMgSi Alloys.* Materials Forum, 2004. **28**: p. 32-46.
7. Lorimer, F.J.H.G.W., *Thermomechanical Processing of Aluminum Alloys*, in *Light Metals and Composites*, R. Ciach, Editor. 1998, Nato Science Partnership Subseries. p. 343-353.
8. Snilsberg, K.E., *Anisotropi i bøyeegenskaper hos utherdbare ekstruderte aluminiumslegeringer*. 2008, Norwegian University of Science and Technology.
9. Graeve, I. and J. Hirsch. *Tempers Overview*. 02.06.14; Available from: http://aluminium.matter.org.uk/content/html/eng/default.asp?catid=214&pageid=2144417057.
10. G. Sha, e.a., *Characterization of Fe-rich Intermetallic Phases in a 6xxx Series Al Alloy.* Materials Science Forum, 2006. **519-521**: p. 1721.
11. Murat, S. and T.T.l. James, *Physical Metallurgy and the Effect of Alloying Additions in Aluminum Alloys*, in *Handbook of Aluminum*. 2003, CRC Press.
12. G. Mrówka-Nowotnik, J.S., M. Wierzbiñska, *Intermetallic phase particles in 6082 aluminum alloy.* Archives of Aluminum Science and Engineering, 2007. **28**(2): p. 69-76.
13. H. Liu, e.a., *Effects of Mn on constituents of Al-Mg-Si-Cu alloys.* The Chinese Journal of Non-Ferrous Metals, 2004. **14**(11): p. 1906-1911.
14. Liu, H., et al., *Effects of magnesium content on phase constituents of Al-Mg-Si-Cu alloys.* Transactions of Nonferrous Metals Society of China, 2006. **16**(2): p. 376-381.
15. Humphreys, F.J. and M. Hatherly, *Recrystallization and related annealing phenomena*. 1995: Elsevier.
16. McQueen, *Hot Deformation and Processing of Aluminum Alloys*. 2011: Taylor and Francis Group.
17. K. Strobel, e.a., *Dispersoid Phases In 6xxx Aluminum Alloys.* Materials Science Forum, 2010. **654-656**: p. 926-929.
18. K. Matsuda, e.a., *Effects of Cu and Transition Metals on the Precipitation Behaviors of Metastable Phases in Al-Mg-Si.* Materials Transactions, 2002. **43**(11): p. 2789-2795.
19. Zhang, J., *Equilibrium pseudobinary Al–Mg2Si phase diagram.* Materials Science and Technology, 2001. **17**(5): p. 494-496.
20. Edwards, G.A., et al., *The precipitation sequence in Al–Mg–Si alloys.* Acta Materialia, 1998. **46**(11): p. 3893-3904.
21. Dieter, G.E., *Mechanical Metallurgy*. 1988: McGraw-Hill.

22. Kato, Y., et al., *Effect of Alloy Elements on Microstructure and Mechanical Properties of Al-Mg-Si Alloys.* 13th International Conference on Aluminum Alloys, 2012.
23. A.K. Gupta, D.J.L., S.A. Court, *Precipitation hardening in Al-Mg-Si alloys with and without excess Si.* Materials Science and Engineering A, 2001. **336**: p. 11-17.
24. Lynch, J.P., L.M. Brown, and M.H. Jacobs, *Microanalysis of age-hardening precipitates in aluminium alloys.* Acta Metallurgica, 1982. **30**(7): p. 1389-1395.
25. J. Aucote, D.W.E., *Effects of excess silicon addition on ductility of Al-0.95%Mg_2Si Alloy.* Materials Science and Technology, 1978. **12**(2): p. 57-63.
26. Chakrabarti, D., Y. Peng, and D.E. Laughlin. *Precipitation in Al-Mg-Si alloys with Cu additions and the role of the Q'and related phases*. in *Materials Science Forum*. 2002. Transtec Publications; 1999.
27. Marioara, C., et al., *The effect of Cu on precipitation in Al–Mg–Si alloys.* Philosophical Magazine, 2007. **87**(23): p. 3385-3413.
28. Matsuda, K., et al., *Precipitation sequence of various kinds of metastable phases in Al-1.0mass% Mg2Si-0.4mass% Si alloy.* Journal of Materials Science, 2000. **35**(1): p. 179-189.
29. Altenpohl, D., *Aluminium und Aluminiumlegierungen*. 1965, Berlin: Springer-Verlag. XIX, 899 s. : ill.
30. Tangen, S., *Deformation and annealing behavior of commercial non-heat treatable aluminium alloys: an experimental investigation*. Vol. 2004:123. 2004, Trondheim: Norges teknisk-naturvitenskapelige universitet. X, 266 s. : ill.
31. Abe, M., K. Asano, and A. Fujiwara, *Influence of the precipitate-free zone width on the tensile properties of an Al-6 Wt pct Zn-1.2 Wt pct Mg alloy.* Metallurgical Transactions, 1973. **4**(6): p. 1499-1505.
32. Kuramoto, S., G. Itoh, and M. Kanno, *Intergranular fracture in some precipitation-hardened aluminum alloys at low temperatures.* Metallurgical and Materials Transactions A, 1996. **27**(10): p. 3081-3088.
33. Ogura T., H.A., Sato T., *Effect of PFZ and Grain Boundary Precipitate On Mechanical Properties and Fracture Morphologies in Al-Zn-Mg(Ag) Alloys.* Materials Science Forum, 2010. **638-642**: p. 297-302.
34. Bridgman, P.W., *Studies in large plastic flow and fracture with special smphasis on the effects of hydrostatic pressure*. Metallurgy and metallurgical engineering series. 1952: McGraw. 362p.illus.,bibl.
35. Chuong J. M., C.S.R., *Study on true stress correction from tensile tests.* Materials Science and Technology, 2008. **22**: p. 1039-1051.
36. G. Le Roy., J.D.E., G. Edward, M. F. Ashby, *A Model of Ductile Fracture Based on the Nucleation and Growth of Voids.* Acta Metallurgica, 1981. **29**: p. 1509-1522.
37. T. Hirose, H.T., M. Ando, T. Suzuki, A. Kohyama, Y. Katoh, M. Narui, *Evaluation of Fatigue Properties with Miniature Hourglass Specimen.* Small Specimen Test Techniques, 2002. **4**.
38. Ling, Y., *Uniaxial True Stress-Strain after Necking.* AMP Journal of Technology, 1996. **5**: p. 37-48.
39. Gilat, A., T.E. Schmidt, and A.L. Walker, *Full Field Strain Measurement in Compression and Tensile Split Hopkinson Bar Experiments.* Experimental Mechanics, 2009. **49**(2): p. 291-302.
40. G. Owolabi, D.O., A. Peterson, A. Odeshi, H. Whitworth, *Measurement of the Deformation of Aluminum Alloys under High Strain Rates Using High Speed Digital Cameras.* World Journal of Mechanics, 2013. **3**: p. 112-121.

41. Askeland, D.R., *The Science and Engineering of Materials*. 2008: Cengage Learning.

42. *Illustration of a ductile fracture*. 10.06.14; Available from: http://www.weck.ca/figs/NucleationGrowthCoalescence.jpg.

43. Hosford, W.F., *Mechanical behavior of materials*. 2010: Cambridge University Press.

44. Hjelen, J., *Scanning elektron-mikroskopi*. 1989: Metallurgisk institutt, NTH.

45. J. K. Solberg, V.H., *Innføring i transmisjon elektronmikroskopi*, N. Department of Materials Science and Engineering, Editor. 2007.

46. *Feature-Specific Measurements*, in *The Image Processing Handbook, Fifth Edition*, J.C. Russ, Editor. 2006, CRC Press. p. 544-597.

47. T. Ferreira, W.R., *ImageJ User Guide IJ 1.46r*. 2012.

48. Williams, D. and C.B. Carter, *The Transmission Electron Microscope*, in *Transmission Electron Microscopy*. 1996, Springer US. p. 3-17.

49. Remøe, M.S., *The Influence of Fe on the Strength and Ductility of 6xxx Al-Mg-Si Alloys*. 2013, NTNU.

50. Cuniberti, A., et al., *Influence of natural aging on the precipitation hardening of an AlMgSi alloy.* Materials Science and Engineering: A, 2010. **527**(20): p. 5307-5311.

Appendix A Constituent distribution in 250X

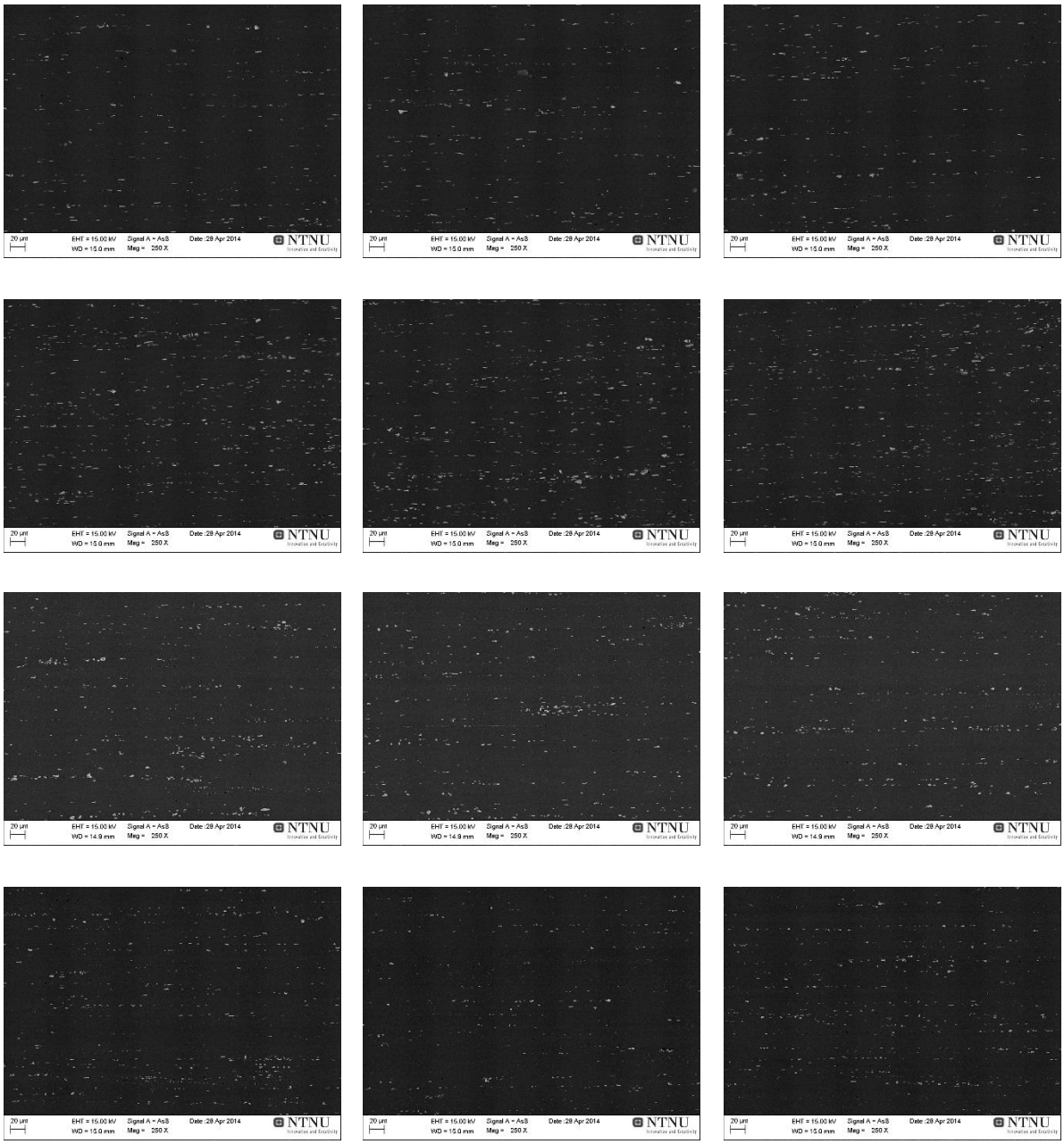

Figure A.1: The images (250X magnification) used for the particle distribution analysis. Each row displays the three images used for each alloy. Row 1: 6181. Row 2: KFC. Row 3: 6082. Row 4: KK13.

Appendix B EDS analysis

1.

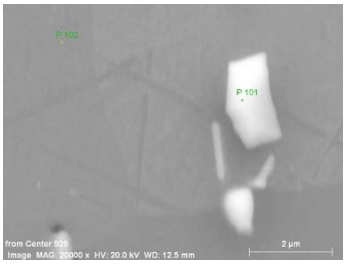

Element	Mg	Al	Si	Fe
Particle	1.25	85.95	4.86	7.94
Matrix	1.50	97.64	0.84	0.01

2.

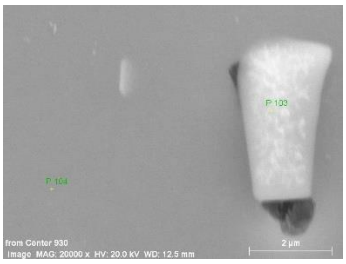

Element	Mg	Al	Si	Fe
Particle	1.57	78.16	11.01	9.26
Matrix	1.47	97.58	0.85	0.10

3.

Element	Mg	Al	Si	Fe
Particle	1.14	75.89	11.93	11.03
Matrix	1.52	97.66	0.81	0.01

4.

Element	Mg	Al	Si	Fe
Particle	1.34	84.39	7.01	7.26
Matrix	1.52	97.67	0.80	0.01

5.

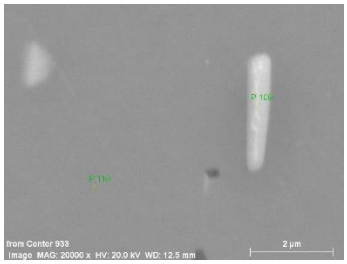

Element	Mg	Al	Si	Fe
Particle	1.41	87.42	6.18	4.99
Matrix	1.53	97.67	0.80	0.00

6.

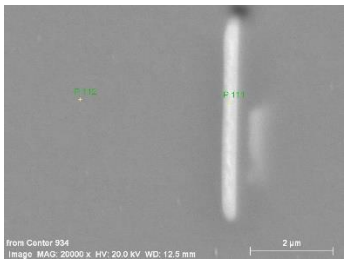

Element	Mg	Al	Si	Fe
Particle	1.60	83.71	7.06	7.63
Matrix	1.53	97.65	0.81	0.01

7.

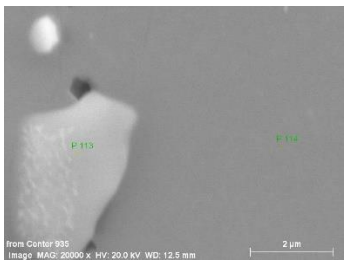

Element	Mg	Al	Si	Fe
Particle	1.71	82.87	8.95	6.46
Matrix	1.53	97.65	0.81	0.00

8.

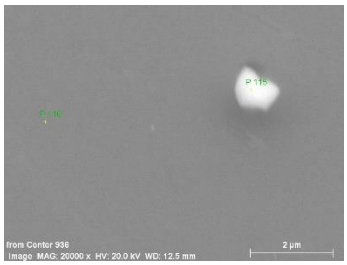

Element	Mg	Al	Si	Fe
Particle	2.34	81.87	6.86	8.93
Matrix	1.55	97.64	0.81	0.01

Figure B.1: EDS analysis of constituents in 6181.

1.

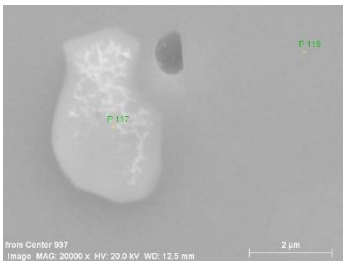

Element	Mg	Al	Si	Fe	Cu
Particle	1.22	83.72	7.96	6.60	0.50
Matrix	1.63	97.37	0.77	0.01	0.22

2.

Element	Mg	Al	Si	Fe	Cu
Particle	1.52	83.40	6.86	7.84	0.38
Matrix	1.59	97.37	0.71	0.02	0.31

3.

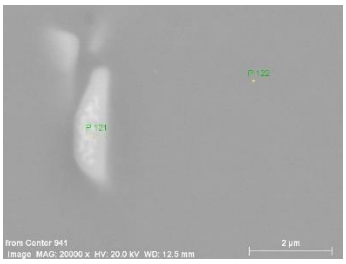

Element	Mg	Al	Si	Fe	Cu
Particle	1.29	77.98	9.31	10.71	0.71
Matrix	1.56	97.42	0.69	0.02	0.31

4.

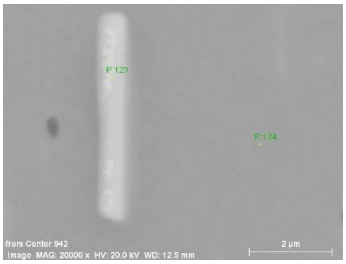

Element	Mg	Al	Si	Fe	Cu
Particle	1.29	81.01	8.42	8.77	0.52
Matrix	1.57	97.41	0.70	0.01	0.31

5.

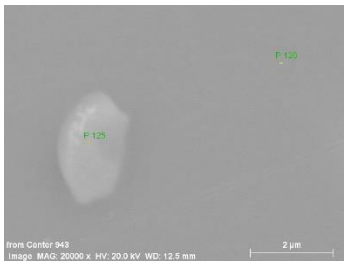

Element	Mg	Al	Si	Fe	Cu
Particle	1.39	86.64	6.47	5.11	0.39
Matrix	1.55	97.44	0.67	0.02	0.31

6.

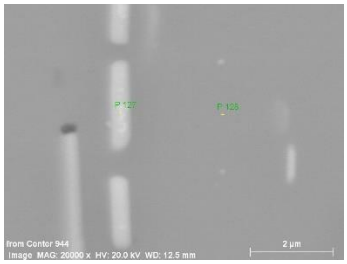

Element	Mg	Al	Si	Fe	Cu
Particle	1.49	82.84	7.98	7.14	0.54
Matrix	1.55	97.43	0.70	0.01	0.30

7.

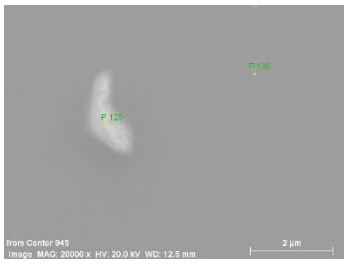

Element	Mg	Al	Si	Fe	Cu
Particle	1.40	84.38	6.85	6.81	0.55
Matrix	1.56	97.42	0.70	0.01	0.31

8.

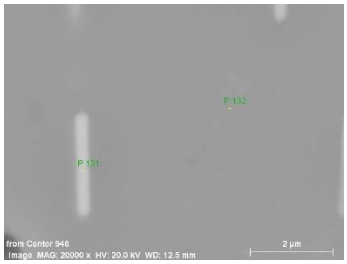

Element	Mg	Al	Si	Fe	Cu
Particle	1.43	83.96	6.67	7.55	0.38
Matrix	1.57	97.43	0.69	0.01	0.30

Figure B.2: EDS analysis of constituents in KFC.

1. 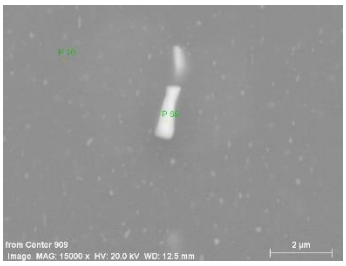

Element	Mg	Al	Si	Mn	Fe
Particle	1.41	84.20	5.25	4.69	4.45
Matrix	1.48	97.51	0.82	0.15	0.03

2. No image

Element	Mg	Al	Si	Mn	Fe
Particle	1.41	83.12	5.53	4.16	5.77
Matrix	1.42	96.41	0.98	0.71	0.48

3. 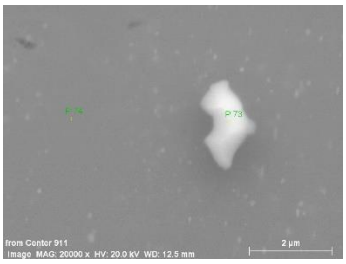

Element	Mg	Al	Si	Mn	Fe
Particle	1.11	81.06	6.06	5.88	5.88
Matrix	1.50	97.61	0.80	0.07	0.02

4. 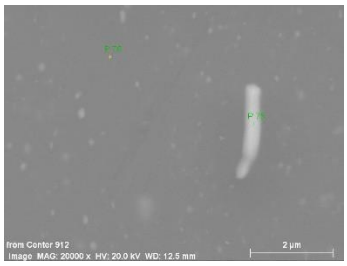

Element	Mg	Al	Si	Mn	Fe
Particle	1.45	88.93	4.03	3.37	2.22
Matrix	1.50	97.62	0.80	0.07	0.02

5. 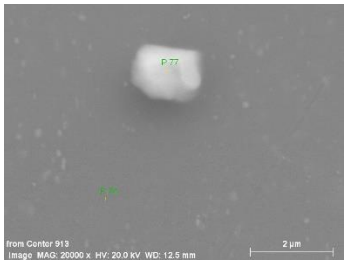

Element	Mg	Al	Si	Mn	Fe
Particle	1.14	82.06	5.66	4.94	6.20
Matrix	1.50	97.56	0.78	0.12	0.04

6. 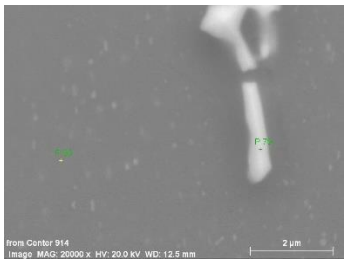

Element	Mg	Al	Si	Mn	Fe
Particle	1.20	83.90	5.08	4.74	5.07
Matrix	1.50	97.41	0.84	0.19	0.05

Figure B.3: EDS analysis of constituents in 6082.

1.

Element	Mg	Al	Si	Mn	Fe	Cu
Particle	1.76	86.75	3.93	2.67	4.33	0.56
Matrix	1.90	97.25	4.10	0.00	0.17	#N/A

5.

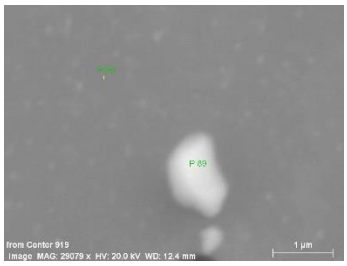

Element	Mg	Al	Si	Mn	Fe	Cu
Particle	1.74	85.04	4.11	3.12	5.35	0.64
Matrix	1.91	97.14	0.53	0.22	0.03	0.18

2.

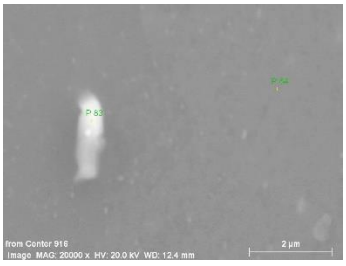

Element	Mg	Al	0.00	Mn	Fe	Cu
Particle	1.71	85.11	0.00	3.34	5.14	0.60
Matrix	1.89	97.29	0.50	0.16	0.02	0.15

6.

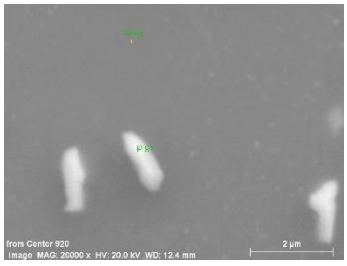

Element	Mg	Al	Si	Mn	Fe	Cu
Particle	1.67	85.14	3.98	3.49	5.13	0.58
Matrix	1.84	97.45	0.46	0.09	0.02	0.14

3.

Element	Mg	Al	Si	Mn	Fe	Cu
Particle	1.68	83.79	4.59	4.14	5.17	0.63
Matrix	1.90	97.22	0.52	0.18	0.03	0.17

7.

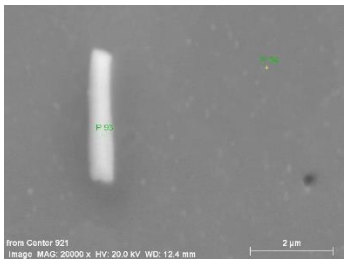

Element	Mg	Al	Si	Mn	Fe	Cu
Particle	1.61	83.17	4.38	3.73	6.42	0.69
Matrix	1.91	97.20	0.51	0.19	0.02	0.17

4.

Element	Mg	Al	Si	Mn	Fe	Cu
Particle	1.69	85.28	4.00	3.16	5.24	0.63
Matrix	1.90	97.22	0.52	0.18	0.02	0.16

8.

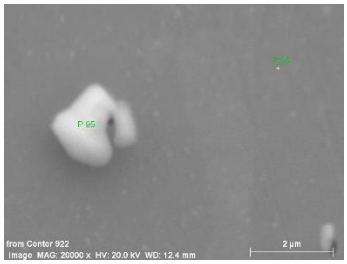

Element	Mg	Al	Si	Mn	Fe	Cu
Particle	1.45	81.64	5.50	4.04	6.67	0.70
Matrix	1.90	97.24	0.52	0.15	0.03	0.17

Figure B.4: EDS analysis of constituents in KK13.

Appendix C Additional TEM images

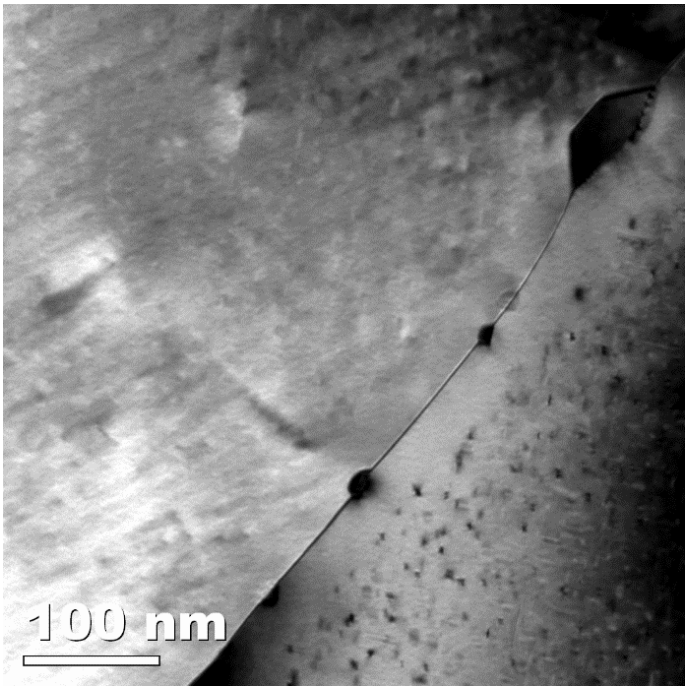

Figure C.1: Grain boundary in KK13 at 40 kX magnification.

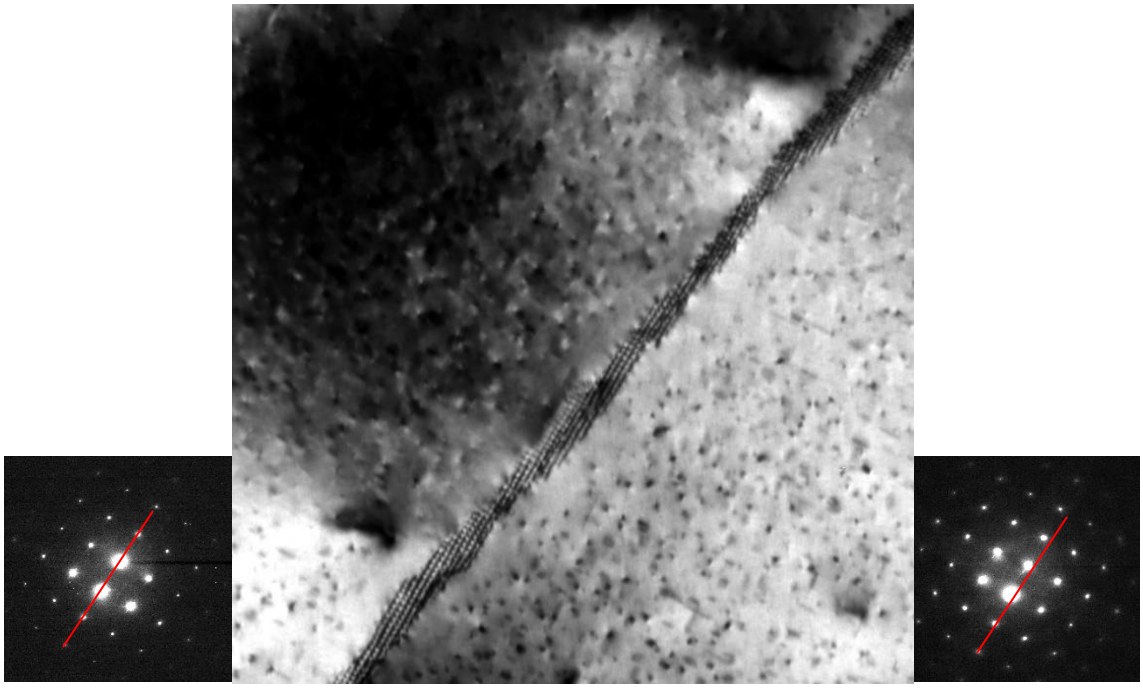

Figure C.2: Moirée fringes in KK13. The red lines (same angle) illustrates the small orientation difference between the grains.

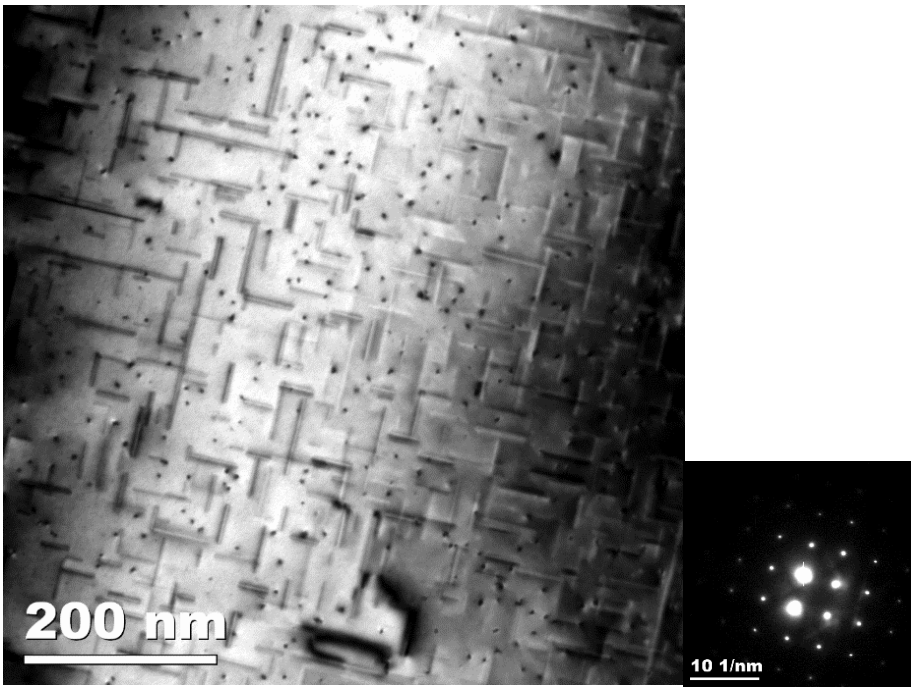

Figure C.3: Precipitates in 6082 at 30kX

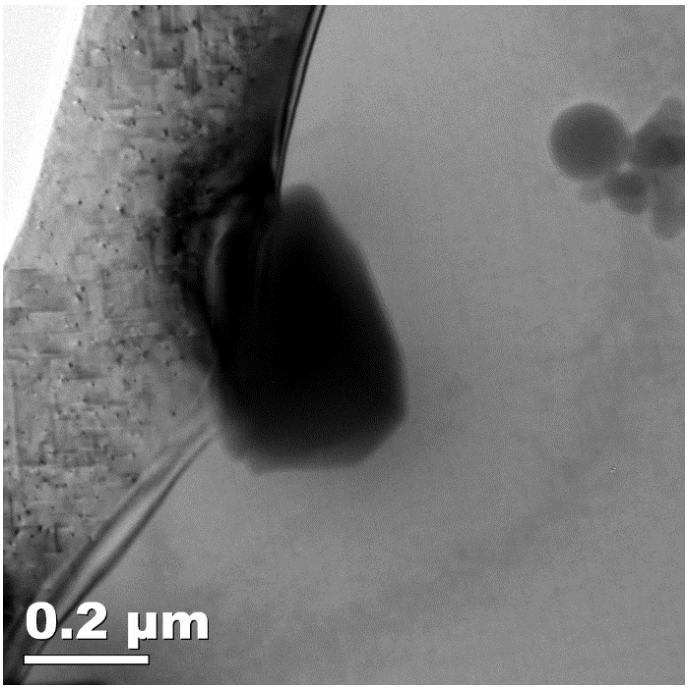

Figure C.4: Dispersoid on a grain boundary in 6181 at 20 kX magnification.

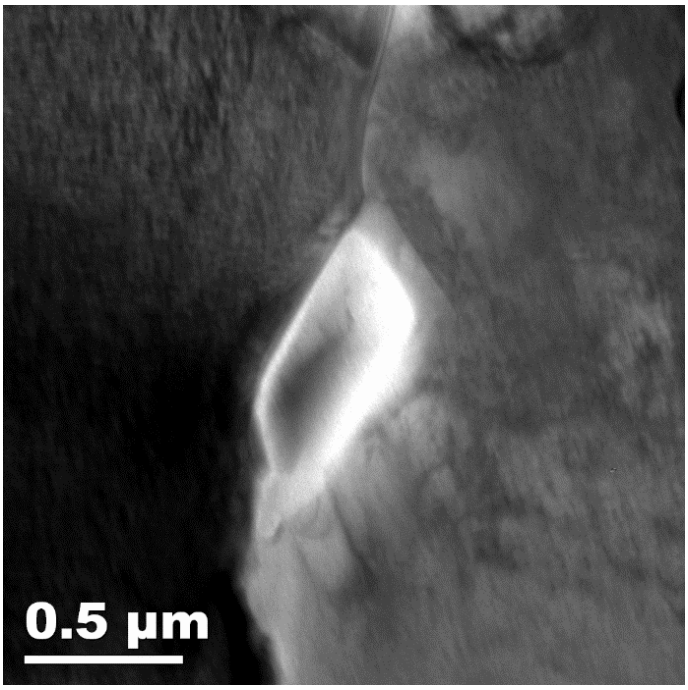

Figure C.5: Dispersoid in 6181 at 10 kX magnification.

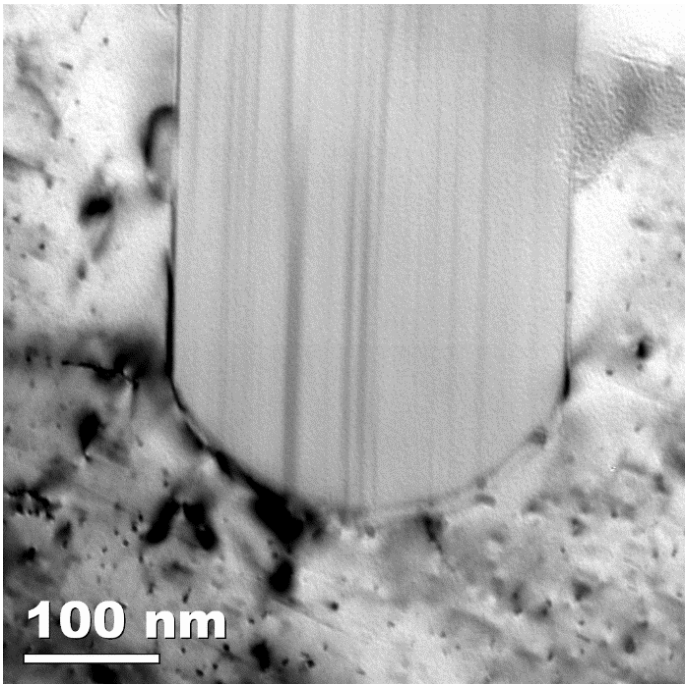

Figure C.6: Dispersoid in KFC at 40 kX magnification.

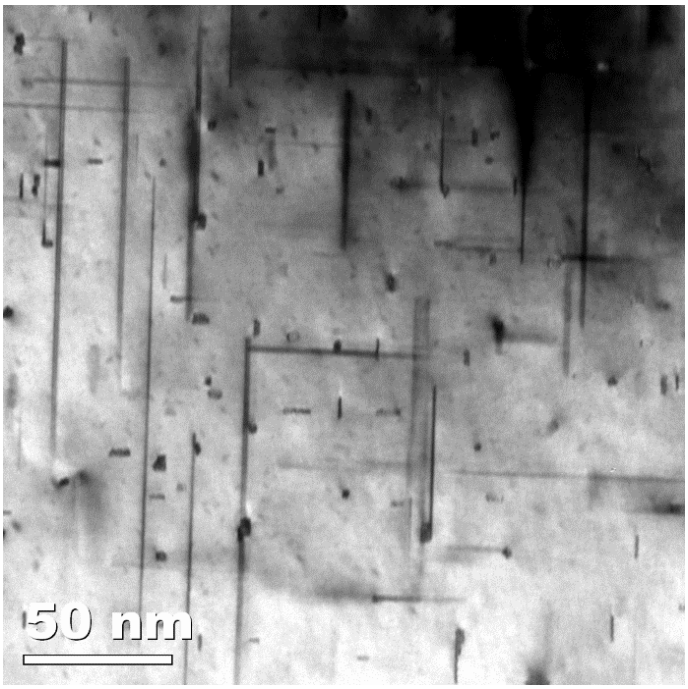

Figure C.7: Precipitates in KFC at 80kX magnification.